

Investigating MPI, two-particle angular
correlation in $e - p$ photoproduction and
assessing resolution and efficiency of the
ePIC detector for EIC

M.Sc. THESIS

by

ROHIT KAUNDAL



DISCIPLINE OF PHYSICS
INDIAN INSTITUTE OF TECHNOLOGY INDORE
INDIA

MAY, 2024

Investigating MPI, two-particle angular
correlation in $e - p$ photoproduction and
assessing resolution and efficiency of the
ePIC detector for EIC

A THESIS

*Submitted in partial fulfillment of the
requirements for the award of the degree*

of

MASTER OF SCIENCE

by

ROHIT KAUNDAL



DISCIPLINE OF PHYSICS
INDIAN INSTITUTE OF TECHNOLOGY INDORE
INDIA
MAY, 2024

Candidate Declaration

I hereby certify that the work which is being presented in the thesis entitled **Investigating MPI, two-particle angular correlation in $e - p$ photoproduction and assessing resolution and efficiency of the ePIC detector for EIC** in the partial fulfillment of the requirements for the award of the degree of **Master of Science** and submitted in the **Discipline of Physics, Indian Institute of Technology Indore**, is an authentic record of my own work carried out during the time period from August 2022 to May 2024 under the supervision of **Prof. Ankhi Roy, Indian Institute of Technology Indore**.

The matter presented in this thesis has not been submitted by me for the award of any other degree of this or any other institute.


24/05/2024

Signature of the student

This is to certify that the above statement made by the candidate is correct to the best of my knowledge.

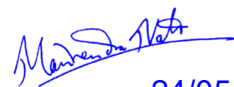

24/05/2024

Signature of Thesis Supervisor

Mr. Rohit Kaundal has successfully given his M.Sc. Oral Examination held on 15 May 2024.


24/05/2024

Signature of Thesis Supervisor


24/05/2024

Convener, DPGC

Acknowledgement

First and foremost, I express my sincere gratitude to my project supervisor, Prof. Ankhi Roy, for her invaluable guidance and unwavering support throughout my research endeavor. I am deeply grateful to all the PhD seniors in my lab, especially Swapnesh bhaiya and Yoshini bhaiya, for their invaluable mentorship and assistance at every juncture. I'm also thankful to my unit mates of VSB-606 for all the colorful memories we've created together. Lastly, I want to thank my parents for always supporting me and believing in me, which kept me focused and motivated.

ROHIT KAUNDAL
MSc., FINAL YEAR
IIT INDORE

All that I am, or hope to be, I owe to my parents

Abstract

The majority of $e - p$ interactions occur via the exchange of photons between them. This interaction manifests in two distinct regimes determined by the virtuality of the exchanged photon: deep inelastic scattering for high virtuality photons and photoproduction for low virtuality (or quasi-real) photons.

This thesis investigates multiple-partonic interactions (MPI) and two-particle correlations in $e - p$ photoproduction across a range of center-of-mass energies from 30 to 318 GeV. Monte Carlo simulations based on the PYTHIA8 event generator are utilized to examine the presence of MPI in $e - p$ photoproduction by comparing PYTHIA8 predictions under various MPI scenarios with experimental data obtained from the ZEUS experiment. In the analysis of two-particle $\Delta\eta - \Delta\phi$ correlations, the ridge structure in $\Delta\eta - \Delta\phi$ space is studied. In the away-side region of $\Delta\phi$ a ridge structure is present in the data and is replicated well by PYTHIA8, although there is no sign of a near-side ridge. Additionally, the variation of correlations with center of mass energy (\sqrt{s}) is studied.

Furthermore, the resolution and efficiency of the ePIC detector for the Electron-Ion Collider (EIC) are assessed using charged hadrons.

Contents

Candidate Declaration	iii
Acknowledgements	v
Abstract	ix
List of Figures	xiii
1 Introduction	1
1.1 Motivation	2
1.2 Structure of the Thesis	5
2 The EIC Experiment	7
2.1 Efficiency of charged hadrons	10
2.2 Efficiency of charged pions	11
2.3 Momentum resolution of charged pions	12
3 Kinematic variables & simulation methodology	17
3.1 Kinematics	17
3.1.1 Kinematic variables in $e - p$ scattering	18
3.1.2 Rapidity and pseudo-rapidity variables	20
3.1.3 Transverse momentum	21
3.2 DIS and photoproduction	21
3.2.1 Photon-proton interaction	24
3.2.2 Multiple partonic interaction	25
3.3 Monte Carlo event generators	25

4	Results and analysis	29
4.1	Transverse momentum and charged multiplicity distribution	29
4.2	Two-particle azimuthal correlation	31
4.3	Energy dependent analysis of transverse momentum and multiplicity distribution	35
4.4	Energy dependent analysis of two-particle correlation . . .	37
4.4.1	$\Delta\eta - \Delta\phi$ correlation	40
5	Summary	47
A	PYTHIA 8 settings for photoproduction	49
B	Mixed event correction	51

List of Figures

1.1	Multi-partonic interactions (MPI) vs average charged multiplicity in $e - p$ photoproduction at $\sqrt{s} = 318$ GeV	3
1.2	Charged particle multiplicity distribution at $\sqrt{s} = 7$ TeV, using PYTHIA8 compared with the experimental data from the ATLAS experiment at LHC	4
2.1	A visual representation depicting the distribution of hadrons and the scattered lepton across the rapidity coverage of the detector, corresponding to different x and Q^2	8
2.2	View of the ePIC detector	9
2.3	p_T distribution of generated particles (left), reconstructed particles (middle) with pseudorapidity range $-4 < \eta < 4$ and reconstructed p_T /generated p_T (right)	10
2.4	η distribution of generated particles (left), reconstructed particles (middle) with p_T range $0 < p_T < 10$ and reconstructed p_T /generated p_T (right)	11
2.5	p_T distribution of generated pions (left), reconstructed pions (middle) with pseudorapidity range $-4 < \eta < 4$ and reconstructed p_T /generated p_T (right)	12
2.6	η distribution of generated pions (left), reconstructed pions (middle) with pseudorapidity range $0 < p_T < 10$ and reconstructed η /generated η (right)	12
2.7	Momentum resolution of charged pions vs generated p_T	13

2.8	Resolution across various p_T ranges, fitted with double gaussian function	14
2.9	Sigma (σ) vs p_T for charged pions	15
3.1	Inelastic electron-proton scattering	18
3.2	Schematic representation of the values of pseudo-rapidity (η) around the detector	21
3.3	(a) Deep inelastic scattering and (b) resolved photoproduction	22
3.4	Comparison of transverse momentum spectra between DIS and photoproduction process at $\sqrt{s} = 318$ GeV	23
3.5	Comparison of charged particle multiplicity distribution between DIS and photoproduction process at $\sqrt{s} = 318$ GeV	24
3.6	Multiple partonic interaction in a nucleon-nucleon collision	25
3.7	Underlying events in a nucleon-nucleon collision	26
4.1	Normalised charged-particle transverse momentum distribution (dN/dp_T) from PYTHIA8 compared to the experimental data from the ZEUS experiment	30
4.2	Normalised charged-particle multiplicity distribution (dN/dN_{ch}) from PYTHIA8 compared to the experimental data from the ZEUS experiment	31
4.3	Two particle azimuthal correlation from PYTHIA8 for different MPIs compared with experimental data from ZEUS (a) $c_1\{2\}$ vs $\Delta\eta$ (b) $c_2\{2\}$ vs $\Delta\eta$	32
4.4	Two particle azimuthal correlation from PYTHIA8 for different MPIs compared with experimental data from the ZEUS experiment (a) $c_1\{2\}$ vs $\langle p_T \rangle$ (b) $c_2\{2\}$ vs $\langle p_T \rangle$	34
4.5	Transverse momentum and charged particle multiplicity distribution of all final state charged particles across various center of mass energies	36
4.6	Two particle azimuthal correlation between all the final state charged particles across various center of mass energies . .	38

LIST OF FIGURES

4.7	Two particle azimuthal correlation between all the final state charged particles across various center of mass energies . . .	39
4.8	$\Delta\eta - \Delta\phi$ correlation of all charge particles at $\sqrt{s} = 318$ GeV	41
4.9	Projection of 2-D correlation function $C(\Delta\eta, \Delta\phi)$, figure 4.8, onto $\Delta\phi$ for $-1.5 < \Delta\eta < 3$ and $-1.5 < \Delta\eta < 1.5$ using PYTHIA8	42
4.10	Projection of 2-D correlation function $C(\Delta\eta, \Delta\phi)$, figure 4.11, onto $\Delta\phi$ across various center of mass energies and for high multiplicity events, simulated using PYTHIA8 . . .	43
4.11	$\Delta\eta - \Delta\phi$ correlation of all charge particles across various center of mass energies, using PYTHIA8	44
(a)	$\Delta\eta - \Delta\phi$ correlation at $\sqrt{s} = 30$ GeV	44
(b)	$\Delta\eta - \Delta\phi$ correlation at $\sqrt{s} = 50$ GeV	44
(c)	$\Delta\eta - \Delta\phi$ correlation at $\sqrt{s} = 75$ GeV	44
(d)	$\Delta\eta - \Delta\phi$ correlation at $\sqrt{s} = 100$ GeV	44
4.12	Near side ($\Delta\phi \approx 0$) and away side ($\Delta\phi \approx \pi$) yield as a function of center of mass energy (\sqrt{s})	45
B.1	Construction of the $\Delta\eta - \Delta\phi$ correlation function. Signal distribution (left), background distribution (middle), and correlation function (right).	51
(a)	Same event correlation	51
(b)	Mixed event correlation	51
(c)	Corrected Correlation	51

Chapter 1

Introduction

Nuclear Science is concerned with the origins and structures of atoms, nuclei, and nucleons, which collectively constitute nearly all the visible mass in the universe. Over decades of study, it has become evident that nucleons consist of even smaller building blocks known as quarks, held together by the strong force mediated by gluons. This fundamental theory describing the strong force is Quantum Chromo-Dynamics (QCD). The objective is to comprehend the intricate interactions among quarks and gluons, and how nucleons and nuclei emerge from the properties and dynamics of these particles. The electron-proton ($e - p$) scattering is the cleaner and precise probe to study the internal structure of the proton.

The majority of ep interactions occur through the exchange of a virtual photon between the electron and the proton. While the interaction of high-energy photons with leptons is well described by electro-weak theory, interactions with hadrons pose challenges and have led to the development of Quantum Chromodynamics (QCD). However, QCD can currently only be solved perturbatively, limiting its applicability to interactions with large momentum transfers between particles. By combining QCD with Quantum Electrodynamics (QED), many aspects of deep inelastic $e - p$ scattering, where the exchanged highly virtual photon acts as a point-like probe to the quark content of the proton, can be described. In contrast, hadronic $\gamma - p$ interactions (photoproduction), involving a real photon or a low-virtuality

exchanged photon, are predominantly soft with low momentum transfer, making them challenging to calculate with perturbative QCD. Measurements of $\gamma - p$ interactions have revealed a hadron-like behavior of the photon [1].

To a first approximation, a photon behaves as an object with a point-like interaction. However, quantum-mechanically, it can fluctuate into a fermion-antifermion pair. These fluctuations, such as into a pair of virtual charged leptons, are described by Quantum Electrodynamics (QED). Additionally, a photon can fluctuate into a $q\bar{q}$ pair with quantum numbers $J^{PC} = 1^{--}$ and charges $Q = S = B = 0$. Interaction between this $q\bar{q}$ pair and a proton occurs if the fluctuation time t_f is large compared to the interaction time t_i [2]. The photon can have three states: the point-like photon, the vector meson state (hadronic state), and the perturbative $q\bar{q}$ pair. The fluctuation of photon into hadronic or $q\bar{q}$ state is called resolved photoproduction.

1.1 Motivation

Multiple distinct initial parton scatterings in a single ep collision can be studied in resolved photoproduction. Such interactions, known as multi-parton interactions (MPI), have been conclusively seen in high-energy $p+p$ and heavy-ion collisions. Now the question is, why we are studying MPI, and why it is important? The answer is that it directly affects particle production, see figure 1.1, as multi-partonic interaction increases the average charged multiplicity increases.

High-multiplicity events are believed to be driven by multi-parton interactions (MPI). Figure 4.2, shows the comparison of the charged particle multiplicity from the ATLAS experiment [3] at LHC to a Monte Carlo model with and without MPI. It is seen that the multiplicity distribution can not be predicted without considering MPI.

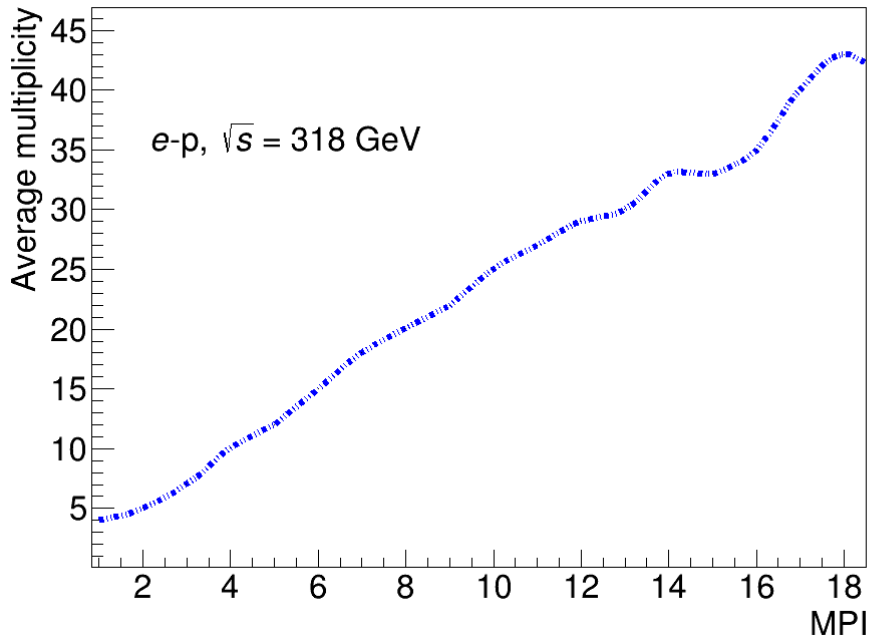


Figure 1.1: Multi-partonic interactions (MPI) vs average charged multiplicity in $e - p$ photoproduction at $\sqrt{s} = 318$ GeV

When two heavy ions collide at high energies, some of their constituent partons may escape from hadronic confinement to form a hot mixture of partons. Often referred to as quark-gluon plasma. It quickly decays into a multihadronic final state, which retains a memory of its origin in terms of correlations between the emerging hadrons. These correlations can be measured by the 2-dimensional plot of particle separation in pseudorapidity (η) and azimuthal angle (ϕ), which shows some interesting features. A strong enhancement of particle pairs with small separation in both η and ϕ signifies the formation of a jet. The presence of a jet and a recoil jet gives the enhancement for pairs of particles to emerge in opposite azimuthal directions. A jet and a recoil jet are not strongly correlated in pseudorapidity, so the opposite azimuth ($\Delta\phi \approx \pi$) particle pairs form a 'ridge' in pseudorapidity difference ($\Delta\eta$). Surprisingly, heavy-ion collisions also show a significant ridge-like component in $\Delta\eta$ in particle pairs with small azimuthal separation ($\Delta\phi \approx 0$). It is also evident in proton-ion and even in proton-proton collisions [4]. This effect is naturally absent in

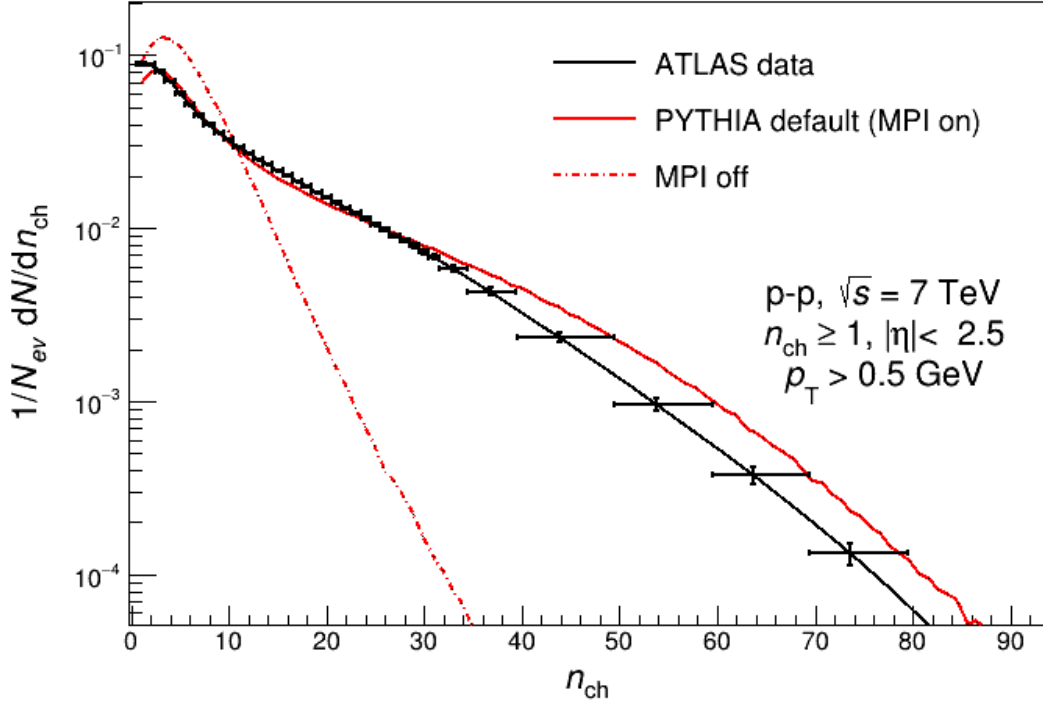


Figure 1.2: Charged particle multiplicity distribution at $\sqrt{s} = 7$ TeV, using PYTHIA8 compared with the experimental data from the ATLAS experiment at LHC

electron-positron collisions [5], so it is interesting to observe whether it is present in electron-proton collisions. And the other thing to see is, whether PYTHIA8 (event generator used to simulate $e - p$ collision events) can reproduce these ridge-like structures.

We have to detect the final state particles precisely to study all the above effects, which requires a detector with very good resolution and efficiency. In particle physics, detectors are the most important. They help us understand what happens during collision experiments. A good detector must be precise and efficient to give us all the details about the particles involved. Before we build a detector, we do simulation studies. These help us to figure out the best design, make sure everything works well, and solve any problems before we start building. Simulations also let us try out different situations that might be tricky or expensive to do in real life. Therefore the study of resolution and efficiency of the detector is crucial for its success.

1.2 Structure of the Thesis

Here we will outline a brief overview of the thesis. This thesis mainly has two parts, in the first part, chapter 2, is dedicated to studying the resolution and efficiency of the ePIC detector for EIC¹. From Chapter 3 we have the phenomenological studies of $e - p$ photoproduction.

- In **chapter 2**, we will discuss briefly the EIC experiment and study the resolution and efficiency of the ePIC detector for EIC.
- **Chapter 3** focuses on the basic kinematics of the $e - p$ collisions, the difference between the deep-inelastic scattering (DIS) and photoproduction, and the event generator used to simulate the collision events.
- **Chapter 4** focuses on results and analysis, in which we have basic kinematic plots (transverse momentum and charged-particle multiplicity), the two-particle azimuthal correlations for different MPIs, compared with the experimental data from ZEUS, and lastly the $\Delta\eta - \Delta\phi$ correlation at various center of mass energies.
- **Chapter 5** is the summary and outlook section of the thesis.
- **Appendix** contains the supplementary information for the reader's reference.

¹Electron-ion collider

Chapter 2

The EIC Experiment

The Electron-Ion Collider (EIC) will be the first collider to explore the inner workings of both protons and nuclei at high energies. It aims to answer fundamental questions about our visible world, such as the origin of nucleon mass, nucleon spin, and properties of dense gluon systems. Using deep inelastic scattering (DIS) processes, the EIC's electron beam will probe protons and nuclei across a wide range of center of mass energy, $\sqrt{s} = 20$ to 140 GeV. This approach offers cleaner data compared to other collision types, enabling precise studies of strong interaction physics. The EIC White Paper outlines key aspects of its extensive physics program [6]. The broad physics of EIC can be accomplished by the study of three basic types of DIS processes:

- **Inclusive DIS:** $e + p/A \rightarrow e' + X$ For this process it is essential to detect the scattered electron, e' , with high precision. All other final state particles are ignored. The scattered electron is critical for processes to determine the event kinematics.
- **Semi-inclusive DIS:** $e + p/A \rightarrow e' + h^{\pm,0} + X$, This process requires measurement of at least one identified hadron with the scattered electron.

- **Exclusive DIS:** $e + p/A \rightarrow e' + p'/A' + \gamma/h^{\pm,0}/VM^1$, This process requires the measurement of all particles in the event with high precision.

All physics processes to be measured at EIC require the measurement of the event (x, Q^2, y, W) and particle kinematics (p_T, z, ϕ, η) (see, section 3.1) reconstructed with high precision. To access the full $x - Q^2$ plane at different center of mass energies and for strongly asymmetric beam energy combinations, the detector must be able to reconstruct events over

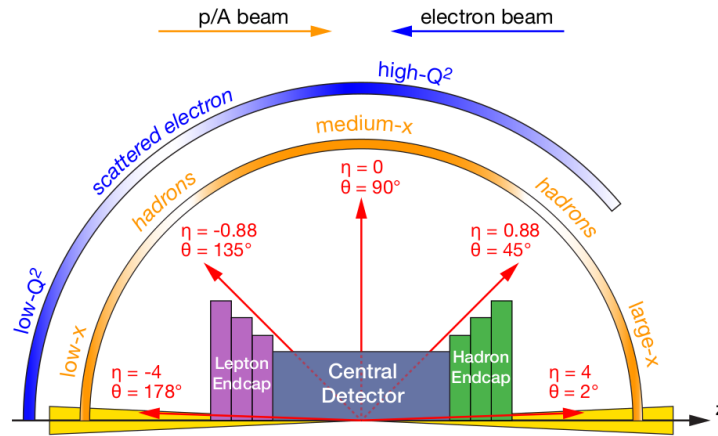


Figure 2.1: A visual representation depicting the distribution of hadrons and the scattered lepton across the rapidity coverage of the detector, corresponding to different x and Q^2

a wide range in η , see figure 2.1 (taken from [7]). This imposes requirements on both detector acceptance and resolution. The central detector, which approximately covers the range of $|\eta| < 1$ is also referred to as a barrel detector, while the hadron end-cap and the electron end-cap are often indicated as forward and backward end-cap, respectively. Figure 2.2 (taken from [8]), we have a view of the first detector of EIC, called ePIC. It is a collection of many sub-detectors. It has a 1.7 Tesla superconducting magnet for curving the trajectories of the charged particles created in collisions, high-precision silicon detectors for tracking particle trajectories

¹Vector Meson

in the magnetic field, precise calorimeters for measuring the energy of the particles, and excellent particle identification detectors.

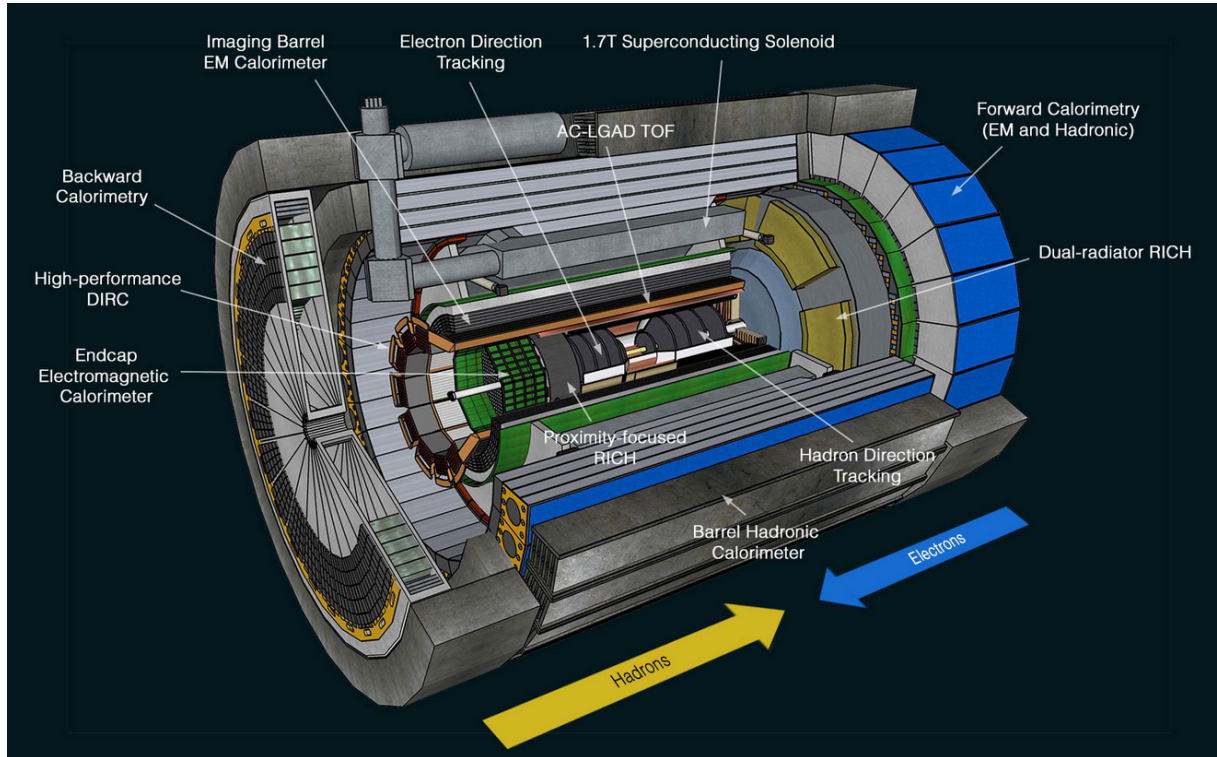


Figure 2.2: View of the ePIC detector

This experimental facility is still in the development phase and the detector is also virtual. So the task that we are doing is to study the resolution and efficiency of the detector so that we can optimize it for better performance. This kind of study is incredibly valuable in the development phase of any experimental facility. This allows us to explore various design parameters, optimize performance, and anticipate potential challenges before committing to physical construction. The process is as follows:

We've obtained data from $e - p$ collisions simulated using the event generator PYTHIA. This data is then passed through our virtual detector setup, yielding output that includes hit positions, energy, momentum, and other relevant information. By comparing the kinematics of the particles generated by PYTHIA with those detected or reconstructed by the virtual detector, we can assess the performance of our detector.

Efficiency is defined as the,

$$Efficiency = \frac{Reconstructed(p_T, \eta, \phi \dots)}{Generated(p_T, \eta, \phi \dots)} \quad (2.1)$$

Resolution is given by,

$$Resolution = \frac{Reconstructed(p_T, \eta, \phi \dots) - Generated(p_T, \eta, \phi \dots)}{Generated(p_T, \eta, \phi \dots)} \quad (2.2)$$

2.1 Efficiency of charged hadrons

In figure 2.3, we have the p_T distribution of both generated and reconstructed charged hadrons, alongside the efficiency depicted by the ratio of reconstructed p_T to generated p_T (right subplot). Notably, the efficiency

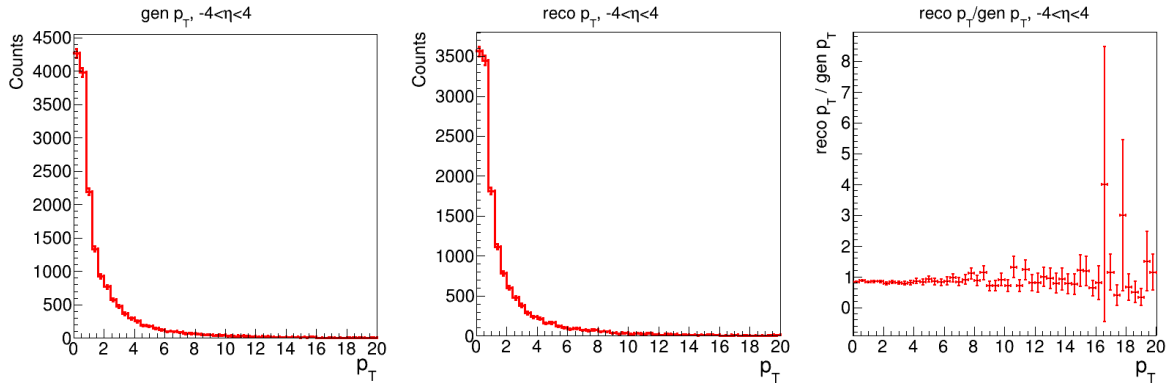


Figure 2.3: p_T distribution of generated particles (left), reconstructed particles (middle) with pseudorapidity range $-4 < \eta < 4$ and reconstructed p_T /generated p_T (right)

plot in figure 2.3 is prominently centered at 1, indicating a high level of accuracy in the reconstruction process. However, at higher p_T , noticeable fluctuations are observed, likely due to the limited statistics.

In figure 2.4, we observe the distribution of η for both generated and

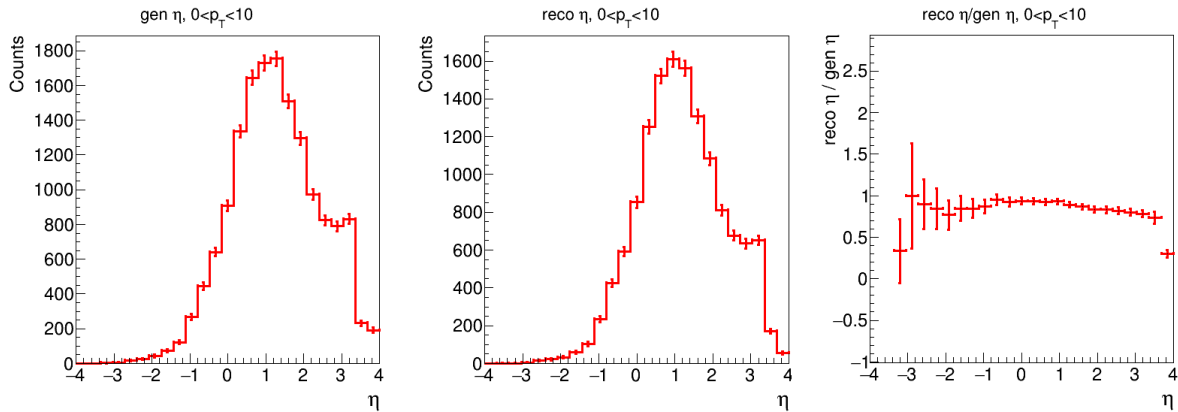


Figure 2.4: η distribution of generated particles (left), reconstructed particles (middle) with p_T range $0 < p_T < 10$ and reconstructed p_T /generated p_T (right)

reconstructed charged hadrons, as well as the efficiency represented by the ratio of reconstructed η to generated η (right subplot). Notably, the efficiency plot in figure 2.4 is prominently centered at 1, indicating a high degree of accuracy in the reconstruction process.

2.2 Efficiency of charged pions

In figure 2.5, we observe the distribution of p_T for both generated and reconstructed charged pions, as well as the efficiency represented by the ratio of reconstructed p_T to generated p_T (right subplot). The efficiency plot in figure 2.5 is prominently centered at 1, showing good reconstruction efficiency.

In figure 2.6, we have the distribution of η for both generated and reconstructed charged pions, as well as the efficiency represented by the ratio of reconstructed η to generated η (right subplot). The efficiency plot in figure 2.6 is prominently centered at 1, indicating a high degree of accuracy in the reconstruction process.

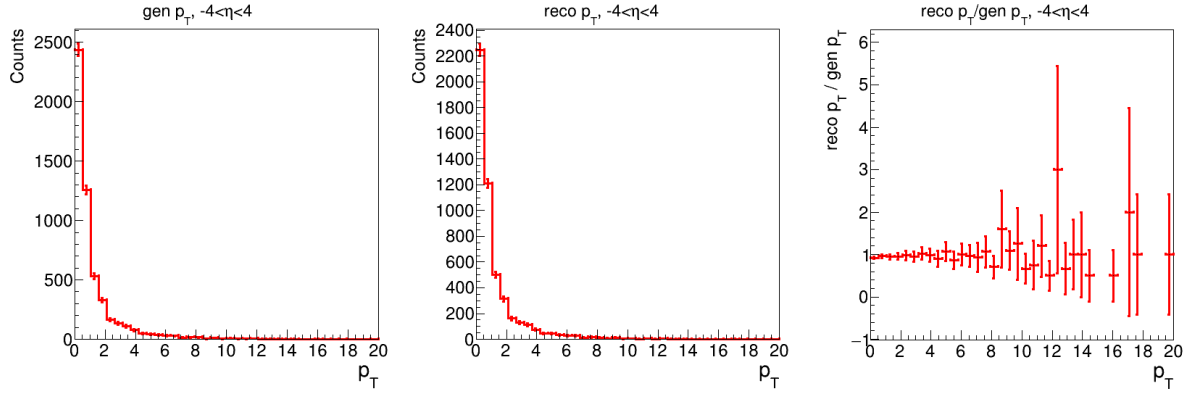


Figure 2.5: p_T distribution of generated pions (left), reconstructed pions (middle) with pseudorapidity range $-4 < \eta < 4$ and reconstructed p_T /generated p_T (right)

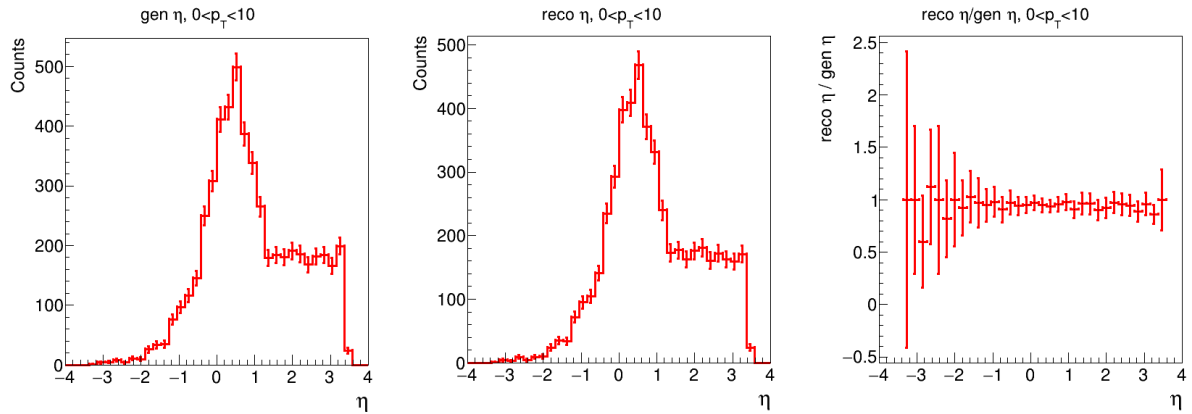


Figure 2.6: η distribution of generated pions (left), reconstructed pions (middle) with pseudorapidity range $0 < p_T < 10$ and reconstructed η /generated η (right)

2.3 Momentum resolution of charged pions

In figure 2.7, we have momentum resolution (see eq-n 2) of charged pions vs generated p_T . It is nicely centered around zero, showing good resolution. In figure 2.8, we have the projection of 2D-histogram, see figure 2.7, onto the Y-axis, for different p_T ranges as shown in the figures 2.8 and these distributions are fitted with the double Gaussian function ² and sigma of each distribution for a particular p_T range is calculated. Sigma (σ) in each

²Double Gaussian function is the sum of two Gaussian functions

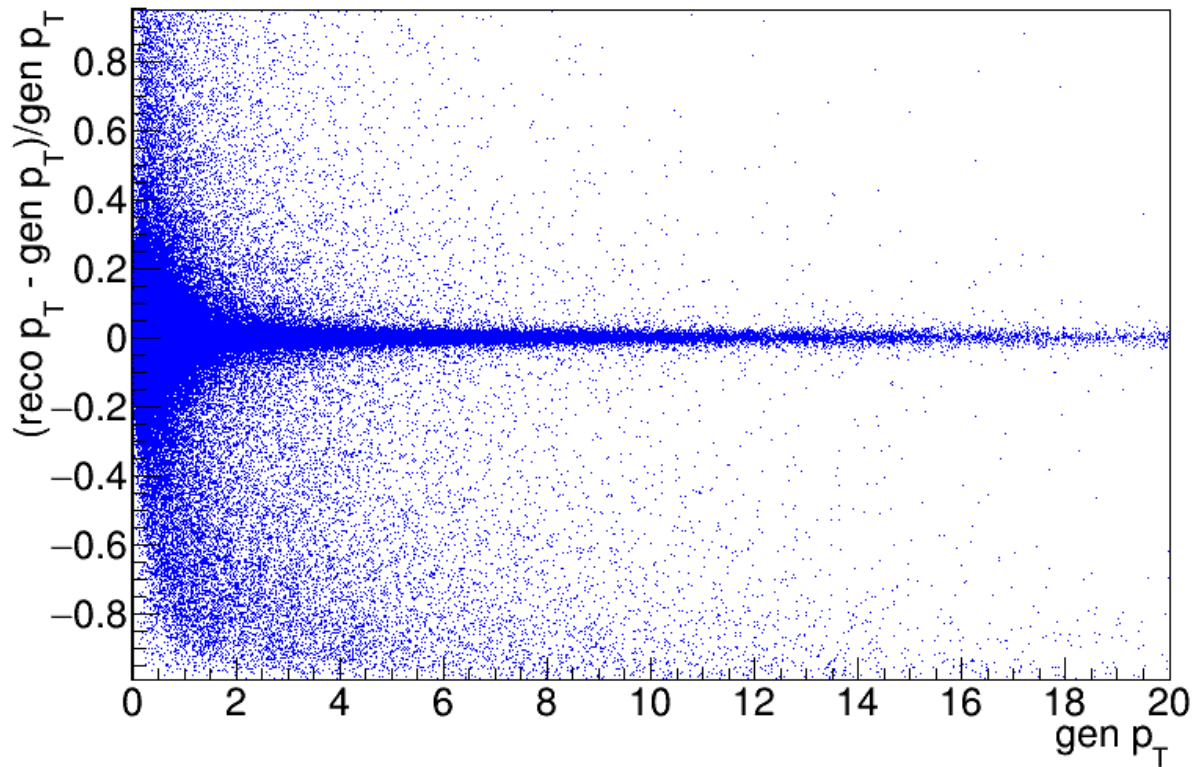
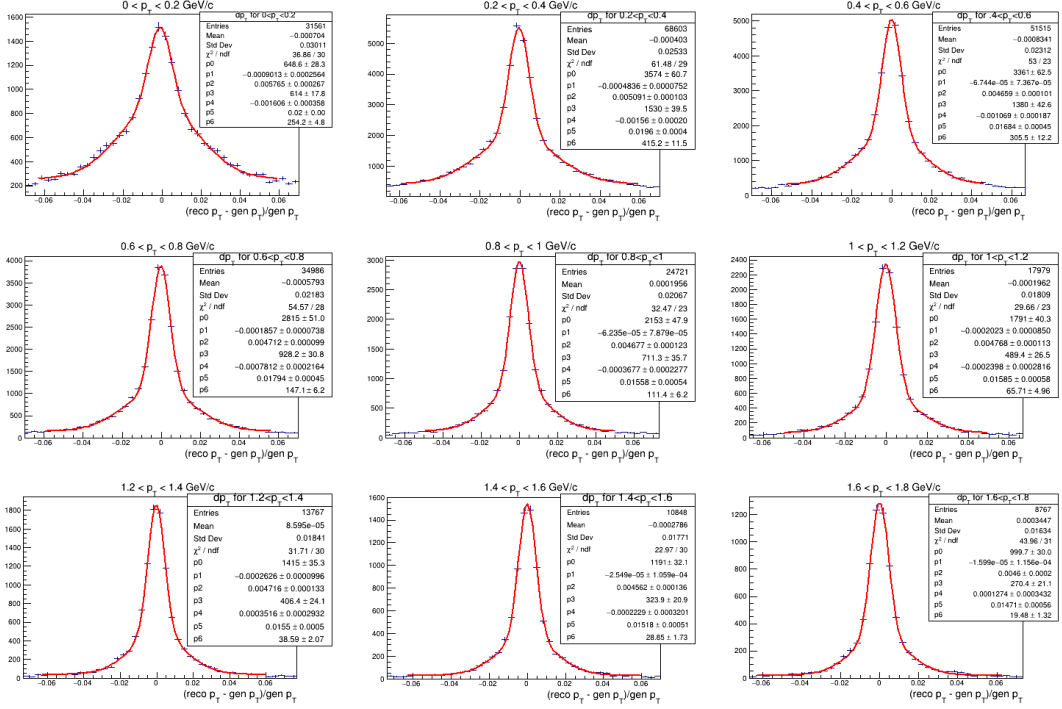


Figure 2.7: Momentum resolution of charged pions vs generated p_T

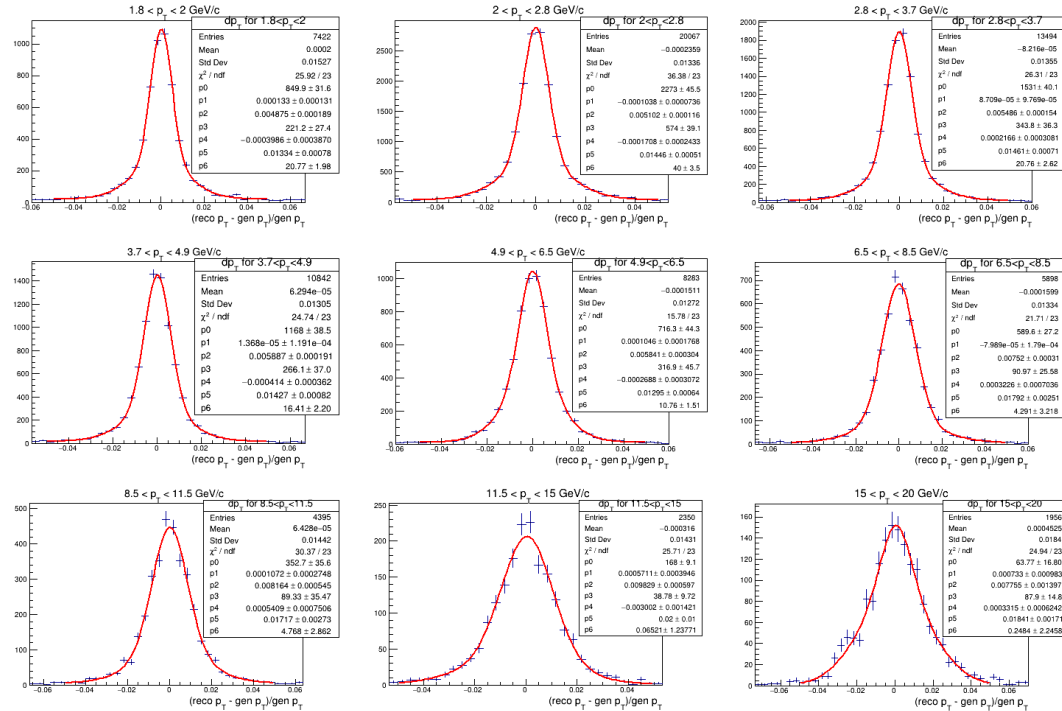
p_T interval show deviations up to 1 %, see figure 2.9. The effective sigma of the double Gaussian function is calculated using,

$$\sigma = \sqrt{\frac{A_1\sigma_1^2 + A_2\sigma_2^2}{A_1 + A_2}} \quad (2.3)$$

here σ_1 , σ_2 and A_1 , A_2 are the standard deviations and amplitudes of each Gaussian function, respectively.

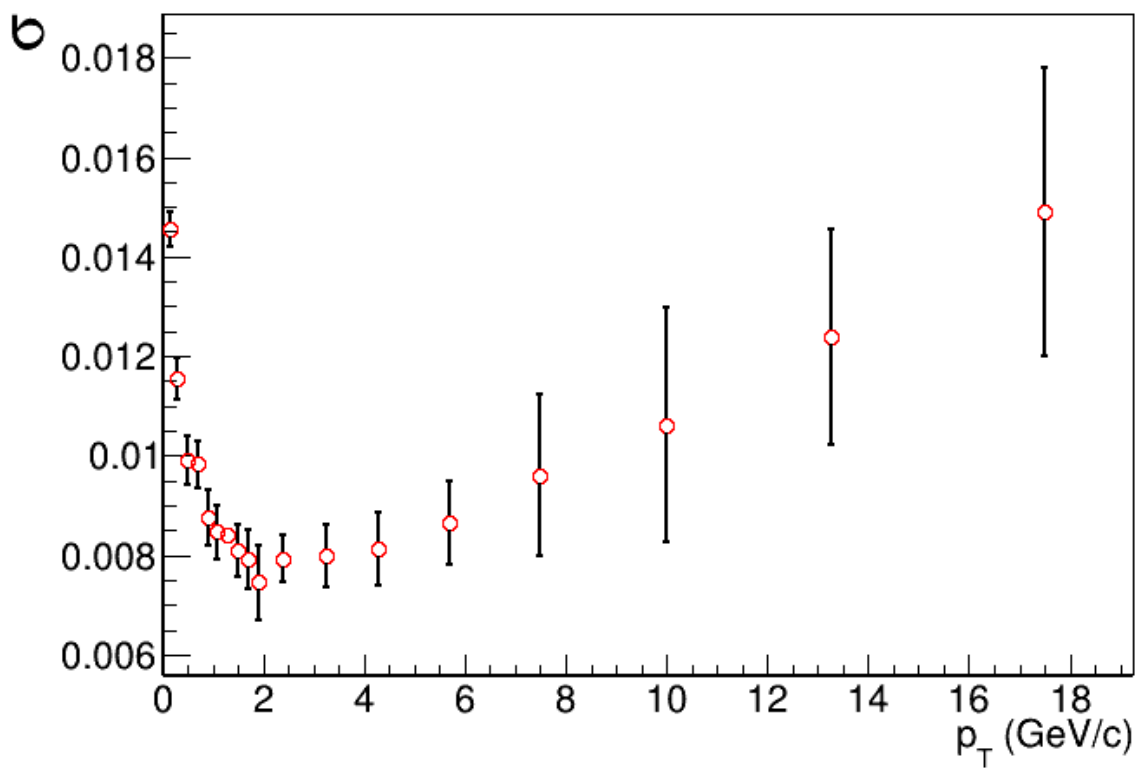


(a) Momentum resolution across various p_T ranges



(b) Momentum resolution across various p_T ranges

Figure 2.8: Resolution across various p_T ranges, fitted with double gaussian function

Figure 2.9: Sigma (σ) vs p_T for charged pions

Chapter 3

Kinematic variables & simulation methodology

In this chapter, the focus lies on examining the kinematic variables involved in $e-p$ collisions. We explore the distinctive characteristics of deep-inelastic scattering and photoproduction, highlighting how these two regimes of $e-p$ scattering differ. Furthermore, the event generator used to simulate the $e-p$ collision events will be discussed.

3.1 Kinematics

The DIS process of an electron with a proton can be written as

$$e(p_1) + p(p_2) \rightarrow e'(p_3) + X(p_4)$$

where e, p refers to the incident electron and proton, e' is the scattered electron and X is the system of particles that are produced in this interaction. p_1, p_2, p_3 and p_4 are their corresponding four momenta. The kinematic variables x, Q^2, y and W^2 described below have intuitive physical interpretations.

3.1.1 Kinematic variables in $e - p$ scattering

Figure 3.1, shows a diagram of an electron-proton collision. In this diagram, the initial four momenta of the electron and proton are labeled p_1 and p_2 respectively and four momenta of the final particles are labeled p_3 and p_4 . Here p_4 is the collective four-momentum of all the particles broke from the proton.

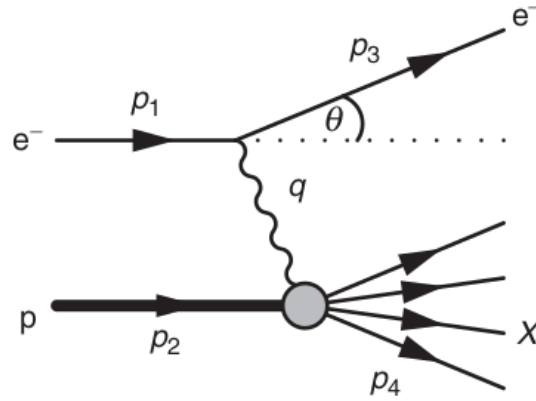


Figure 3.1: Inelastic electron-proton scattering

The momentum transfer that occurs between the electron and the proton manifests as the exchange of a virtual photon with a four-momentum of $q = p_1 - p_3$. To simplify calculations across reference frames, the Lorentz invariant quantity q^2 is used to describe the momentum transfer. Yet, q^2 is a negative quantity, so the convention is to use a positive value labeled as Q^2 , where

$$Q^2 = -q^2 \quad (3.1)$$

Q^2 , is always positive.

The Lorentz invariant dimensionless quantity **Bjorken** x

$$x \equiv \frac{Q^2}{2 p_2 \cdot q} \quad (3.2)$$

will turn out to be an important kinematic variable in the discussion of the quark model of deep inelastic scattering. In the quark-parton model,

Bjorken x can be identified as the fraction of momentum of the proton carried by the parton inside the proton.

The invariant mass of the outgoing hadronic constituents is

$$W^2 \equiv p_4^2 = (p_2 + q)^2 \quad (3.3)$$

W is also the CM energy of γp system, therefore x becomes

$$x = \frac{Q^2}{Q^2 + W^2 - m_p^2} \quad (3.4)$$

m_p is the mass of the proton, $W^2 \equiv p_4^2 \geq m_p^2$ and $Q^2 \geq 0$, we have

$$\boxed{0 \leq x \leq 1} \quad (3.5)$$

The value of x is the measure of "elasticity" of the scattering process.

Another dimensionless Lorentz invariant quantity is, y .

$$y \equiv \frac{p_2 \cdot q}{p_2 \cdot p_1} \quad (3.6)$$

In the frame where the proton is at rest, $p_2 = (m_p, 0, 0, 0)$ and momentum of the virtual photon, $q = (E_1 - E_3, \mathbf{p}_1 - \mathbf{p}_3)$ and therefore,

$$y = 1 - \frac{E_3}{E_1} \quad (3.7)$$

E_1 and E_3 are the energies of incoming and scattered electron respectively.

It is easy to see that,

$$\boxed{0 \leq y \leq 1} \quad (3.8)$$

y is the fraction of energy lost by the electron in the rest frame of the proton.

In the lab frame, it is given by,

$$y = 1 - \frac{E_3}{E_1} \cos^2 \frac{\theta}{2} \quad (3.9)$$

3.1.2 Rapidity and pseudo-rapidity variables

At relativistic energy, the rapidity variable is defined as,

$$y = \frac{1}{2} \ln \left(\frac{E + p_z}{E - p_z} \right) = \frac{1}{2} \ln \left(\frac{1 + p_z/E}{1 - p_z/E} \right) \quad (3.10)$$

$$y = \tanh^{-1} \left(\frac{p_z}{E} \right) \quad (3.11)$$

It is a more appropriate quantity than the longitudinal velocity ($\beta_l = \frac{p_z}{E}$). The advantage of rapidity is that it is additive under a longitudinal boost and the difference between the rapidities of two particles is invariant for the boost along the z-axis.

The relationship between the rapidity y of a particle in the laboratory frame F and the rapidity y' in a boosted frame F' which moves with a velocity β in the z - direction is,

$$y' = y - \frac{1}{2} \ln \left(\frac{1 + \beta}{1 - \beta} \right) \quad (3.12)$$

The only problem with rapidity is that we have to measure the energy and momentum of the particle, which is not easy. This leads to the concept of pseudo-rapidity.

For a particle emitted at an angle θ to the beam axis, the rapidity is given by,

$$y = \frac{1}{2} \ln \left(\frac{E + p_z}{E - p_z} \right) = \frac{1}{2} \ln \left(\frac{\sqrt{m^2 + p^2} + p \cos \theta}{\sqrt{m^2 + p^2} - p \cos \theta} \right) \quad (3.13)$$

at very high energy, $p \gg m$, mass can be neglected,

$$y = \frac{1}{2} \ln \left(\frac{p + p \cos \theta}{p - p \cos \theta} \right)$$

$$y = -\ln \tan(\theta/2) \equiv \eta \quad (3.14)$$

η is called pseudo-rapidity. For this only θ measurement is required. It is a convenient parameter for experiments when details of the particle, e.g. mass, momentum, etc. are not known, but only the angle of emission is known, see figure 3.2. For $\eta = 0$, we have θ with respect to beam axis is 90° and for $\theta = 0$ or 180° , η is large.

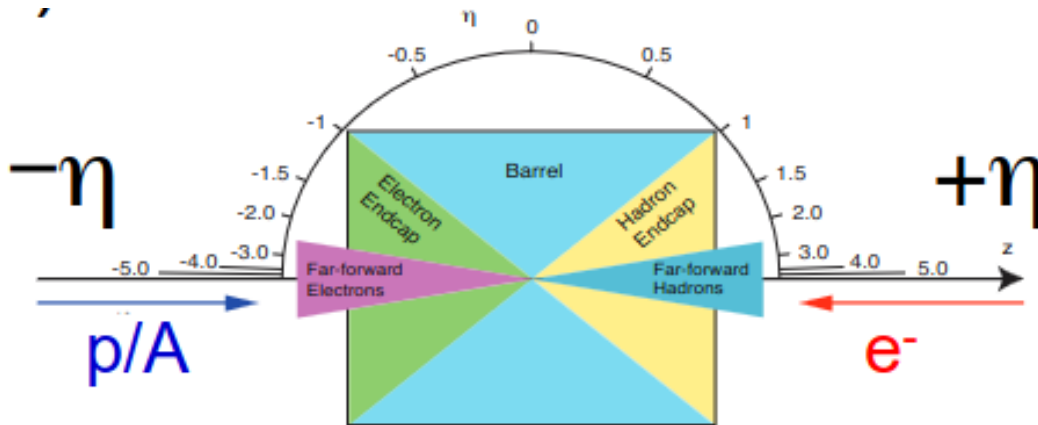


Figure 3.2: Schematic representation of the values of pseudo-rapidity (η) around the detector

3.1.3 Transverse momentum

As the name suggested, transverse momentum is the transverse or perpendicular component of the total momentum of a particle with respect to the beam axis (z -axis). It is denoted by p_T , and given by

$$p_T = \sqrt{p_x^2 + p_y^2}$$

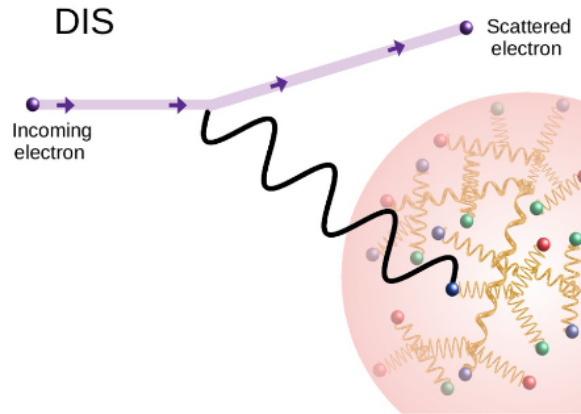
Transverse momentum is a key factor in understanding collisions. It provides insights into the initial conditions of the collision and the behavior of particles during and after the collision. Before a collision, there's no sideways momentum. But after the collision, any sideways movement a particle has comes from the collision itself. So, by looking at how much sideways momentum particles have, we can learn a lot about what happened during the collision. We'll explore this idea further in the upcoming sections.

3.2 DIS and photoproduction

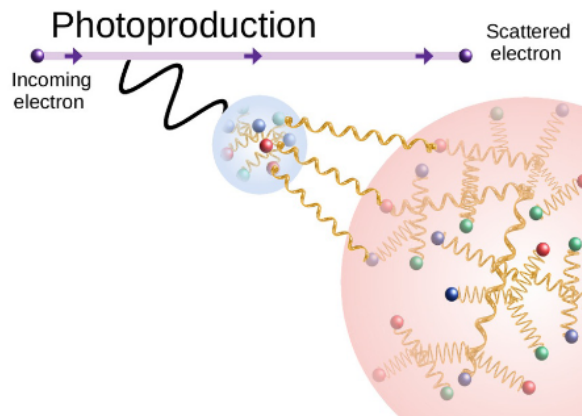
In deep inelastic scattering (DIS), where the momentum transfer carried by the photon between the electron and proton is high, $Q^2 \gg 1 \text{ GeV}^2$, the photon is considered to couple directly to the parton content of the proton,

see figure 3.3a. In DIS, the photon is treated as a point particle. The high Q^2 allows the quark parton model and perturbative QCD to describe the interaction in terms of the structure of the proton. At low Q^2 another technique is required.

For real photons, $Q^2 \approx 0$, or photons of low virtuality, $Q^2 < 1 \text{ GeV}^2$, these



(a) Neutral currents deep inelastic scattering (NC DIS)



(b) Resolved photoproduction

Figure 3.3: (a) Deep inelastic scattering and (b) resolved photoproduction

interactions with the proton are well described by treating the photon as a particle that may have a hadronic structure.

The $e - p$ interaction may be conceptually broken down into two parts, $ep \rightarrow e' + \gamma p$ and $\gamma p \rightarrow X$. In the first, the electron is considered to be accompanied by a flux of virtual photons. At low virtualities, the exchanged γ can be shown to behave like a real photon, thus the second part is true

photoproduction.

The important thing to notice is that we do not have experimental control over the values of Q^2 , so how do we know experimentally, that the $e - p$ scattering process happening is DIS or Photoproduction? For this notice, the figure 3.3 (taken from [9]), in the case of DIS the scattered electron is deflected through a large angle, on the other hand in photoproduction the scattered electron is almost collinear with the incident electron. Experimentally photoproduction and DIS differ by the absence or presence of a scattered electron in the detector system. In photoproduction, the electron typically scatters at small angles and remains very close to the beam pipe and hence remains undetected, while in DIS, the angle of the scattered electron increases with Q_2 , and above a minimum Q_2 , can be efficiently detected. Figure 3.4 compares the p_T spectra of DIS and photoproduction

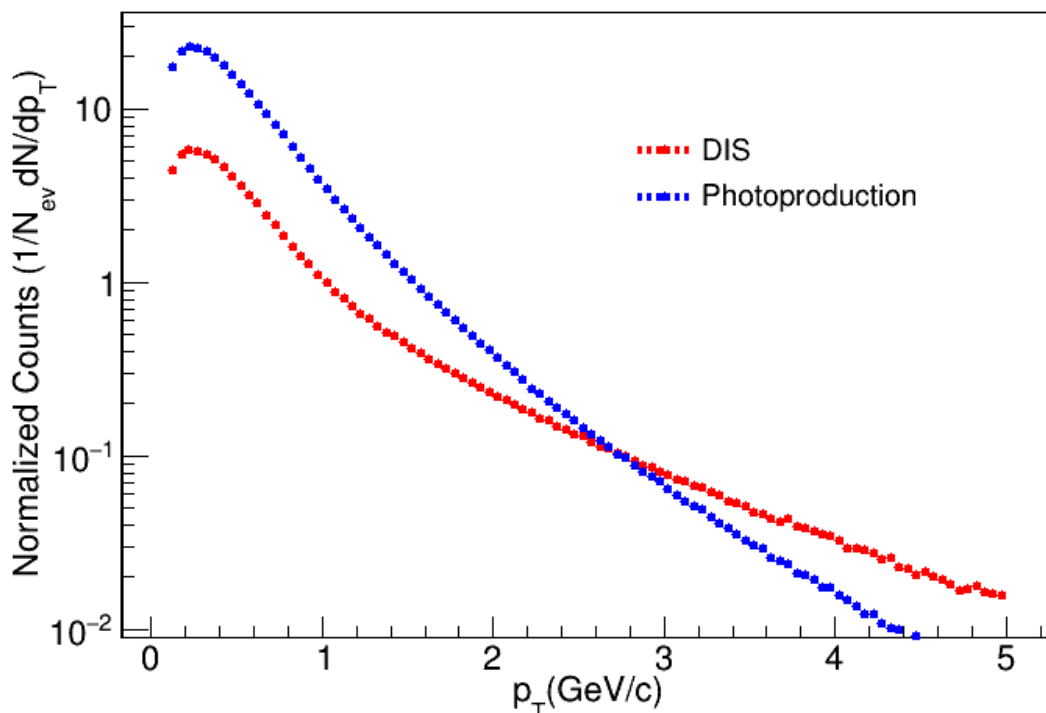


Figure 3.4: Comparison of transverse momentum spectra between DIS and photoproduction process at $\sqrt{s} = 318$ GeV

at $\sqrt{s} = 318$ GeV. In the high p_T region we have more particle production in the case of DIS compared to photoproduction and the low p_T region is

dominated by photoproduction. This is very obvious due to the high Q^2 in the case of DIS compared to photoproduction.

In figure 3.5, we have a comparison of charged particle multiplicity distribution between DIS and photoproduction at $\sqrt{s} = 318$ GeV. Events with high multiplicity are more in photoproduction as compared to DIS. This is because of the multi-partonic interaction in photoproduction, which enhances particle production.

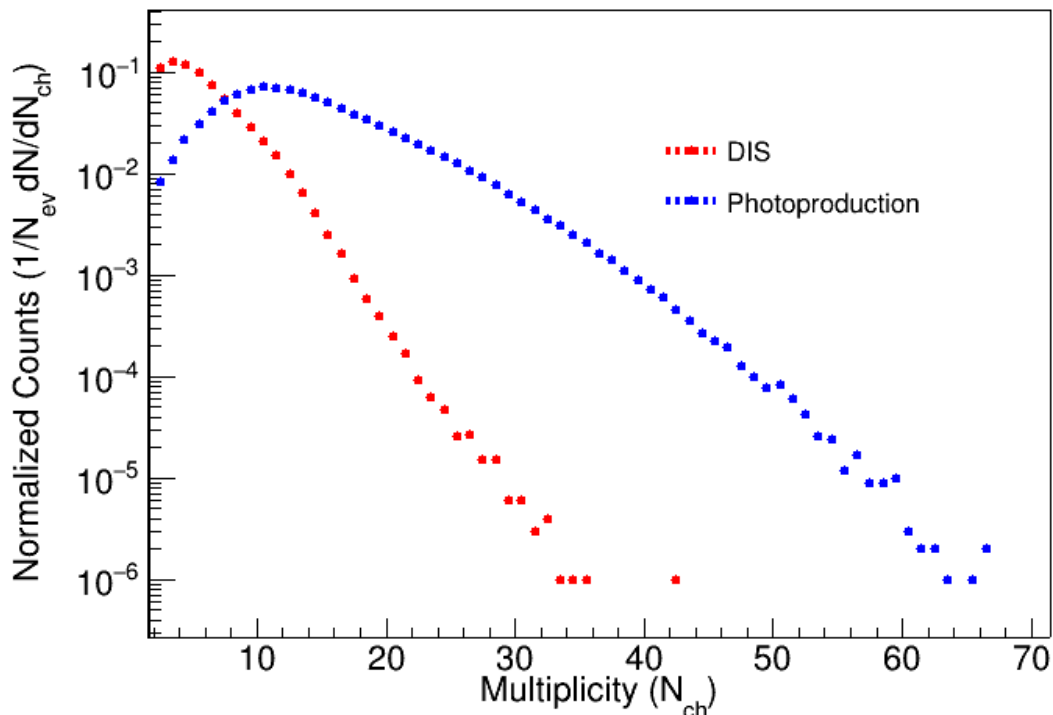


Figure 3.5: Comparison of charged particle multiplicity distribution between DIS and photoproduction process at $\sqrt{s} = 318$ GeV

3.2.1 Photon-proton interaction

The total photoproduction cross-section typically refers to the hadronic interaction of the photon with the proton. High-energy $\gamma - p$ interactions can be classified into three primary event types. The predominant interaction is the interaction of the proton with the hadronic structure of the photon, a phenomenon explained by the vector meson dominance (VMD)

model [1]. Another set of events arises from the direct coupling of the photon to a parton within the proton. A third category of interaction emerges when the photon resolves into a $q\bar{q}$ pair, which then interacts with a parton within the proton. This behavior is often termed the anomalous photon contribution. The total photoproduction cross-section is determined by these mechanisms is given by,

$$\sigma_{tot}^{\gamma p}(W, Q^2) = \sigma_{VMD}^{\gamma p}(W, Q^2) + \sigma_{direct}^{\gamma p}(W, Q^2) + \sigma_{anomalous}^{\gamma p}(W, Q^2) \quad (3.15)$$

where Q^2 is the photon's virtuality and W is γp center of mass energy.

3.2.2 Multiple partonic interaction

A proton is not a point particle, it has a substructure and here we are talking about $e - p$ photoproduction in which the exchanged photon fluctuates into partons. During the collision, the interaction is not just between a photon and one parton (as in the case of DIS) but involves multiple parton-parton interactions. Therefore multipartonic interaction refers to the simultaneous interactions between numerous partons during high-energy collisions. These are primary interactions between multiple partons of the two colliding systems, see figure 3.6.

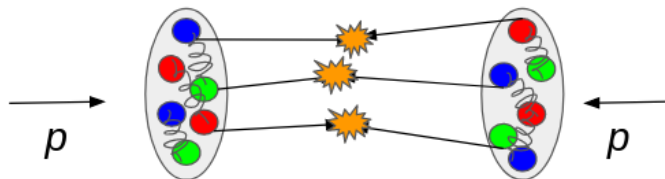


Figure 3.6: Multiple partonic interaction in a nucleon-nucleon collision

3.3 Monte Carlo event generators

The Monte Carlo method is a technique that is used to solve problems using random numbers and probabilities. It's widely used in numerical

analysis and simulating natural processes. In particle physics, Monte Carlo generators create theoretical simulations of real events, helping scientists understand particle interactions in experiments. Different Monte Carlo generators often simulate different physics models, using matrix elements, PDFs, evolution equations, parton showers, or hadronization models. The few major general-purpose event generators are given below

- PYTHIA
- HERWIG
- SHERPA
- ISAJET

In the current study, PYTHIA 8 is used. A detailed description can be found in [10].

In PYTHIA 8 the collision processes (in our case $e - p$ photoproduction) are modeled as a series of sub-processes.

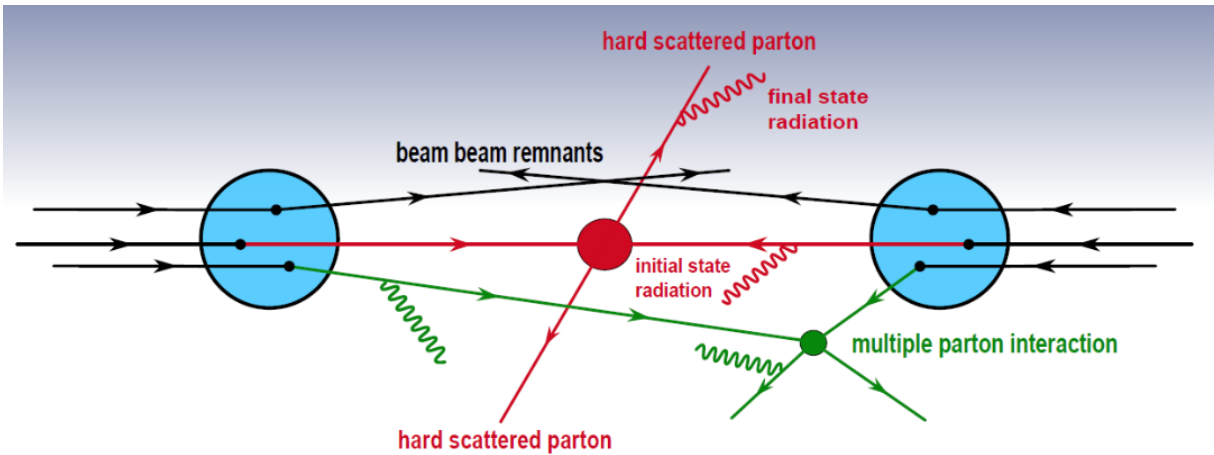


Figure 3.7: Underlying events in a nucleon-nucleon collision

- Hard scattering processes: These processes are characterized by large momentum transfer between the two colliding partons. The outgoing partons from the hard scattering produce a collimated shower

of partons and the process is called fragmentation. Finally, all partons convert themselves into collimated showers of experimentally detectable hadrons, known as jets.

- Initial and final state radiation (ISR): A collision implies accelerated color (and often electromagnetic) charges, and therefore bremsstrahlung can occur. Emissions that are associated with the two incoming colliding partons are called initial state radiation and emission of radiation by outgoing partons are called final state radiation, see figure 3.7.
- Multiple parton interactions (MPI): As explained in 3.2.2, if the colliding particles are composite objects and have more than one parton, then there is a possibility of having more than one parton-parton interactions in a single collision event. This is called multiple-parton interactions (MPI).
- Beam Remnants: Part of the incoming beam that does not take an active part in the initial-state radiation or hard scattering process is called beam remnant, these remnants are then color-connected with the rest of the event. They carry much of the energy of the incoming beam and only a fraction of the energy is taken by the colliding partons.
- Hadronization: The confinement forces become significant as the partons created recede from each other. All the outgoing partons end up confined into hadrons. This process is called hadronization. First principles cannot currently describe the structure and evolution of these force fields, so models have to be introduced. In PYTHIA the hadronization process is governed by the Lund string fragmentation model.

The key parameters utilized to generate photoproduction events are listed in Appendix A.

Chapter 4

Results and analysis

In this chapter, the analysis focuses on Multiple Parton Interactions (MPI), two-particle azimuthal correlation, and $\Delta\eta - \Delta\phi$ correlation. The discussion begins with basic kinematic plots depicting the transverse momentum distribution and multiplicity distribution of all final state charged particles. These plots are compared with experimental data from the ZEUS experiment for different MPI scenarios. Subsequently, a similar comparison is conducted for the two-particle correlation, and the MPI prediction that best matches the data is selected for further analysis. Following this, the $\Delta\eta - \Delta\phi$ correlation is examined.

4.1 Transverse momentum and charged multiplicity distribution

In figure 4.1, the transverse momentum distribution of all final state charged particles is shown for four different MPI settings of PYTHIA8 and these distributions are compared with the experimental data from ZEUS. The center of mass energy of the colliding particles, $e - p$, is 318 GeV, with $Q^2 < 1\text{GeV}^2$. High multiplicity events with $N_{ch} > 20$ (charged multiplicity), particles within $-1.5 < \eta < 2$, and $0.1 < p_T < 5$ GeV/c range are selected. From figure 4.1, it is observed that the PYTHIA8 predictions

with mean MPI ($\langle \text{MPI} \rangle = 1.24$) explain the experimental data. whereas PYTHIA8 prediction with MPI off is overshooting the data.

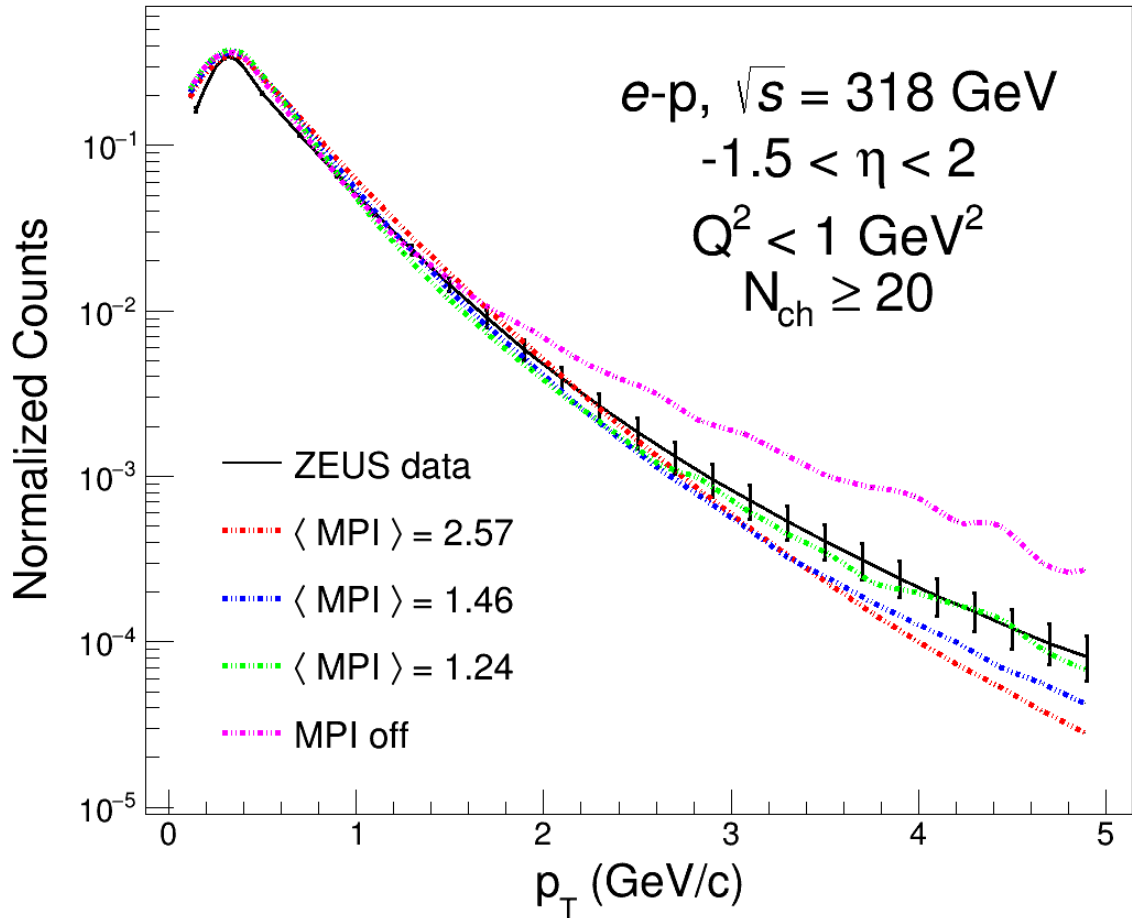


Figure 4.1: Normalised charged-particle transverse momentum distribution (dN/dp_T) from PYTHIA8 compared to the experimental data from the ZEUS experiment

In figure 4.2, the multiplicity¹ distribution of all final state charged particles is shown for four different MPI settings of PYTHIA8 and these distributions are compared with the experimental data from ZEUS. As explained above, the same center of mass energy, $\sqrt{s} = 318$ GeV, and the same kinematic cuts are used. It is observed that the PYTHIA8 predictions with a mean MPI ($\langle \text{MPI} \rangle = 1.24$) explain the experimental data. whereas PYTHIA8 prediction with other MPI settings are not able to explain the

¹Number of particles produced in a collision event

experimental data.

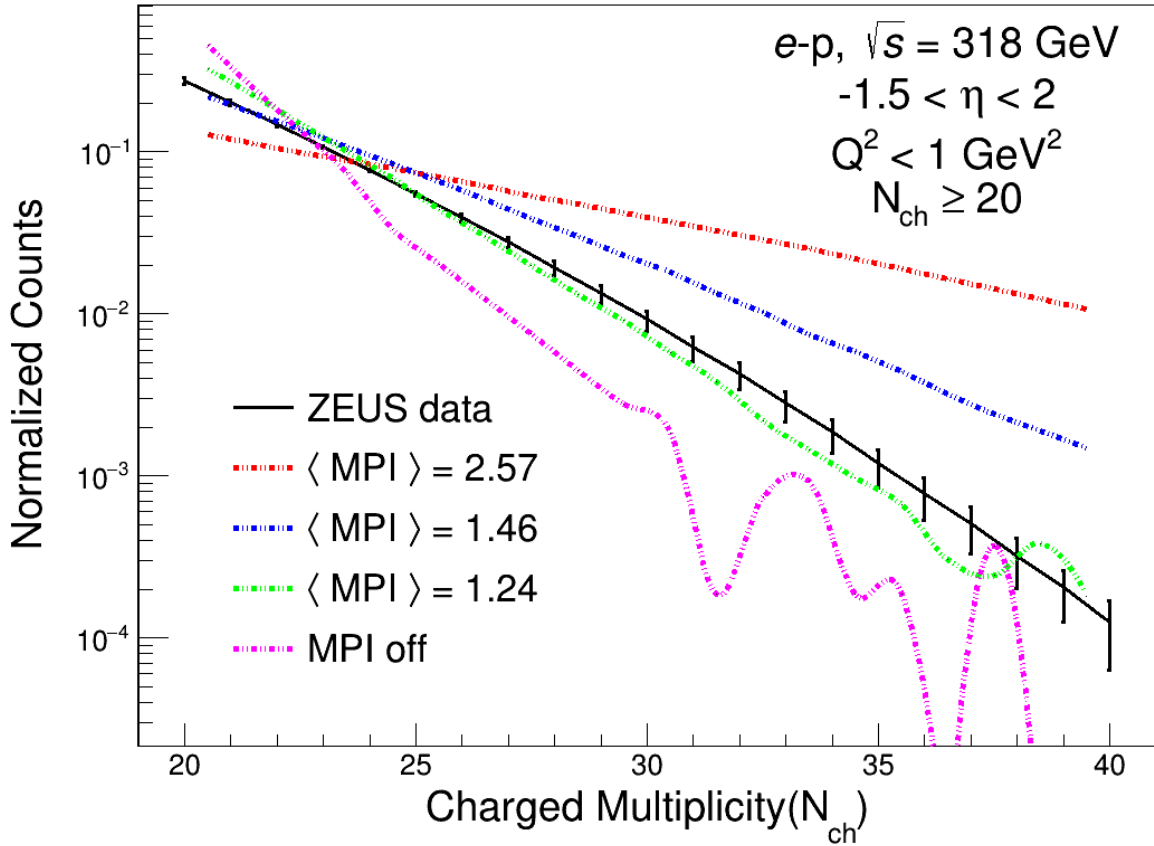
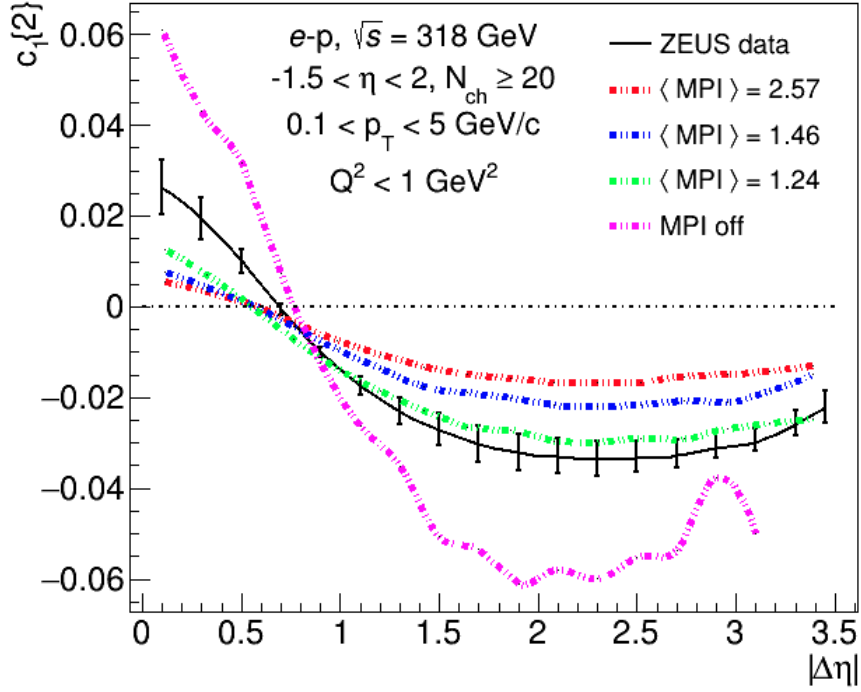


Figure 4.2: Normalised charged-particle multiplicity distribution (dN/dN_{ch}) from PYTHIA8 compared to the experimental data from the ZEUS experiment

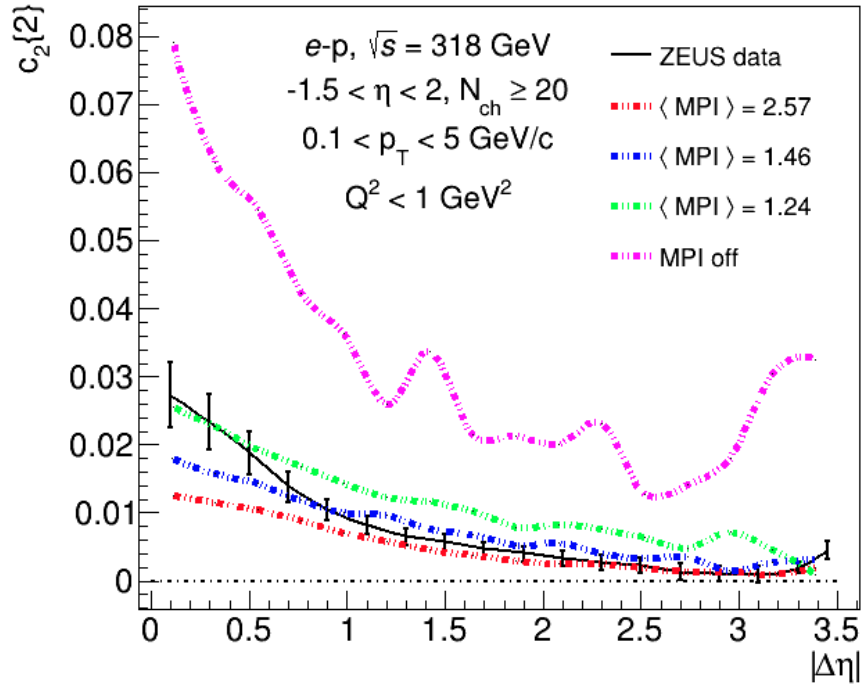
4.2 Two-particle azimuthal correlation

In the two-particle correlation method, the correlations between pairs of particles are used to extract information about the particle's distribution. The basic idea is to make pairs of all the particles within an event and analyze the relative azimuthal angles between these pairs. The correlation function can be expressed as

$$\frac{dN^{pairs}}{d\Delta\phi} \propto \left(1 + \sum_{n=1}^{\infty} 2c_n \cos(n\Delta\phi)\right) \quad (4.1)$$



(a) $c_1\{2\}$ vs $\Delta\eta$



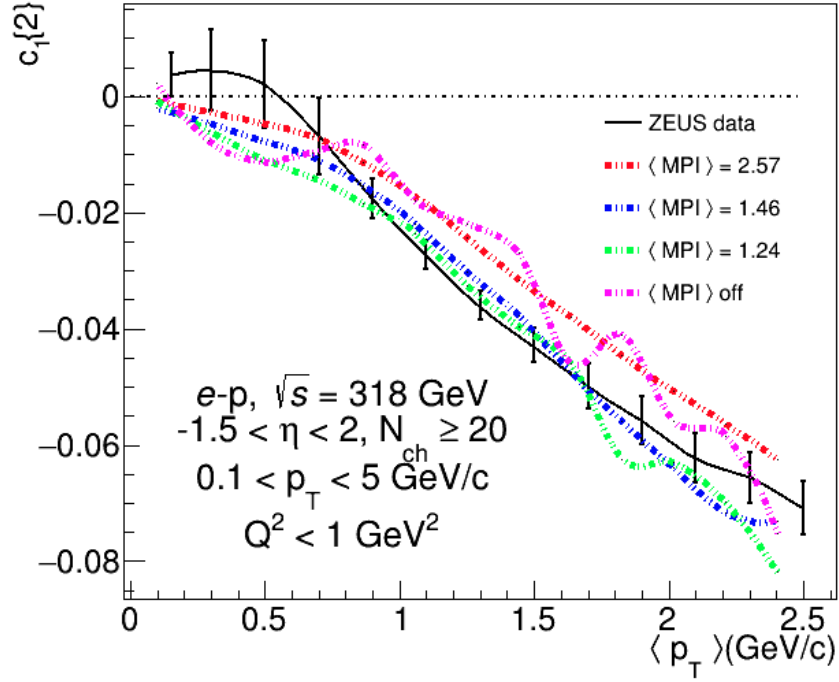
(b) $c_2\{2\}$ vs $\Delta\eta$

Figure 4.3: Two particle azimuthal correlation from PYTHIA8 for different MPIs compared with experimental data from ZEUS (a) $c_1\{2\}$ vs $\Delta\eta$ (b) $c_2\{2\}$ vs $\Delta\eta$

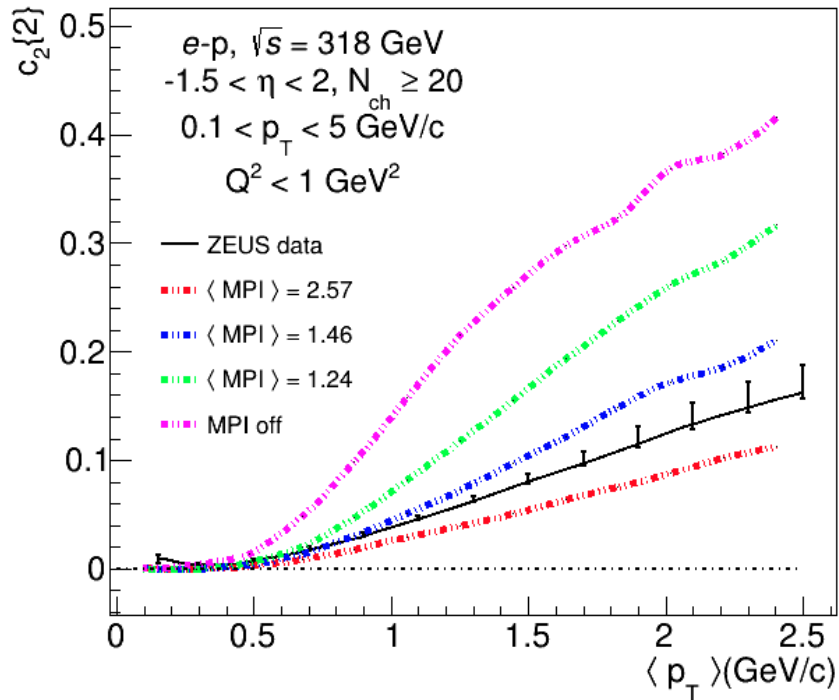
$$c_n\{2\} = \langle \cos[n(\phi_1 - \phi_2)] \rangle \quad (4.2)$$

the angled brackets in the equation 4.2 denoted the average over all the pairs and $\Delta\phi = \phi_1 - \phi_2$ is the difference in the azimuthal angles of the selected pair, particles 1 and 2, n represents the different harmonics of the fourier expansion. We have plotted the fourier coefficients $c_n\{2\}$ with $\Delta\eta = \eta_1 - \eta_2$ and $\langle p_T \rangle = (p_{T1} + p_{T2})/2$.

Figure 4.3, shows the two-particle azimuthal correlation as a function of rapidity separation, $\Delta\eta$, for different MPI settings of PYTHIA8 and compared with the experimental data from ZEUS experiment. Figure 4.3a, shows the $c_1\{2\}$ vs $\Delta\eta$ plot and 4.3b, shows the $c_2\{2\}$ vs $\Delta\eta$ plot for $\sqrt{s} = 318$ GeV, $Q^2 < 1$ GeV², $-1.5 < \eta < 2$ and $0.1 < p_T < 5$ GeV/c. The experimental data from ZEUS is well explained by mean MPI ($\langle \text{MPI} \rangle = 1.24$) as compared to other MPI settings, and the data with MPI off completely disfavored the data, this trend will be seen in all the plots. This strongly suggests the presence of MPI in $e-p$ photoproduction. Similarly, figure 4.4a and 4.4b, show the two-particle azimuthal correlation as a function of average p_T for different MPI, compared with experimental data.



(a) $c_1\{2\}$ vs $\langle p_T \rangle$



(b) $c_2\{2\}$ vs $\langle p_T \rangle$

Figure 4.4: Two particle azimuthal correlation from PYTHIA8 for different MPIs compared with experimental data from the ZEUS experiment (a) $c_1\{2\}$ vs $\langle p_T \rangle$ (b) $c_2\{2\}$ vs $\langle p_T \rangle$

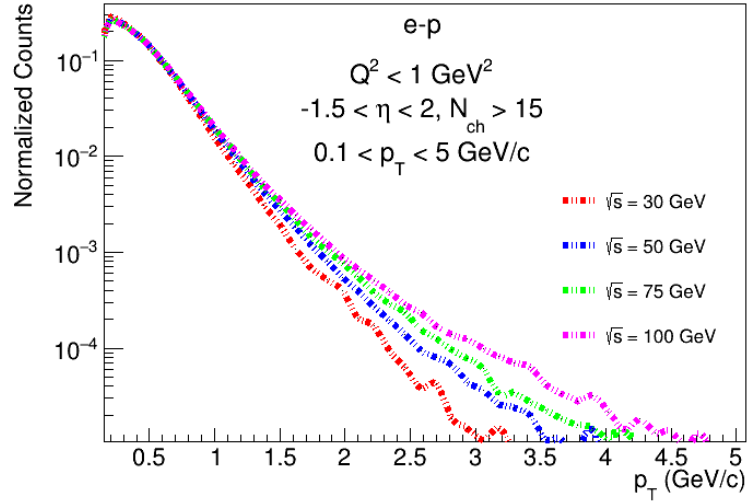
From the discussion so far, we can conclude that MPI is present in $e - p$ photoproduction, as the data with MPI off consistently fails to match the experimental data. Additionally, PYTHIA8 predictions with mean MPI values of 1.2 to 1.4 closely resemble the experimental data. But note that in PYTHIA8 the MPI is controlled by a parameter p_{T0} , which is a lower cut-off on partons momenta, and the energy dependence of p_{T0} is parameterized as $p_{T0} = p_{T0}^{ref} (W/7TeV)^{0.215}$, here W is the center of mass energy of the γp system, see Appendix A. So the MPI will change with the change in the center of mass energy. For $p_{T0}^{ref} = 4$ GeV/c the corresponding value of mean MPI at $\sqrt{s} = 318$ GeV is 1.24.

In the next section, we will examine how basic kinematic variables (such as p_T and multiplicity distribution) and correlations change with the center-of-mass energy. Moving forward, we will use $p_{T0}^{ref} = 4$ GeV/c, which explains the experimental data. In the future, we will have a new experimental facility that will collide electrons with protons, with the variable center of mass energy ranging from 20-100 GeV, so we will see how all the above distributions change with energy, especially at EIC energies.

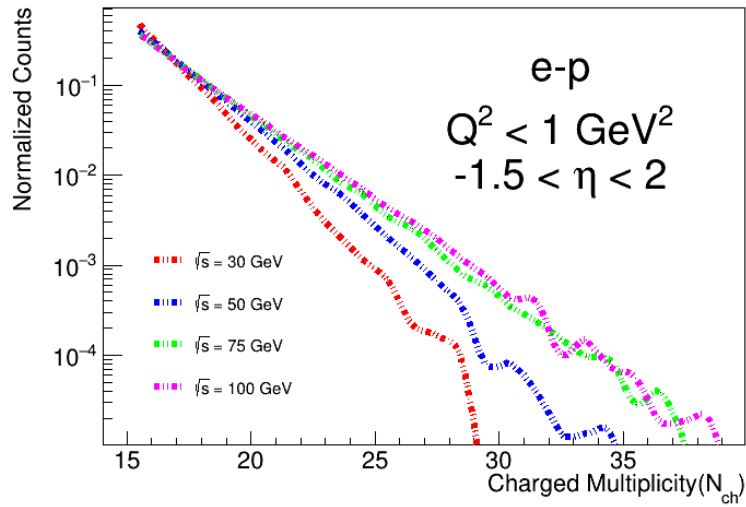
4.3 Energy dependent analysis of transverse momentum and multiplicity distribution

Figure 4.5a and 4.5b, we have transverse momentum and multiplicity distribution of all final state charged particles for variable energy. The distribution is normalized by the total number of particles or entries, which we have within kinematic cuts. All the particles are selected within the $-1.5 < \eta < 2$, $0.1 < p_T < 5$ GeV/c and high multiplicity, $N_{ch} > 15$. As the center-of-mass energy increases, overall particle production rises, as evidenced by the observed trend in transverse momentum spectra. Additionally, the particle production per event also escalates with a higher center of mass-energy. This is very obvious because with high energy momentum transfer will be more and also MPI will be more and therefore

particle production will be more, and we have seen in previous sections that MPI enhances particle production.



(a) Transverse momentum distribution



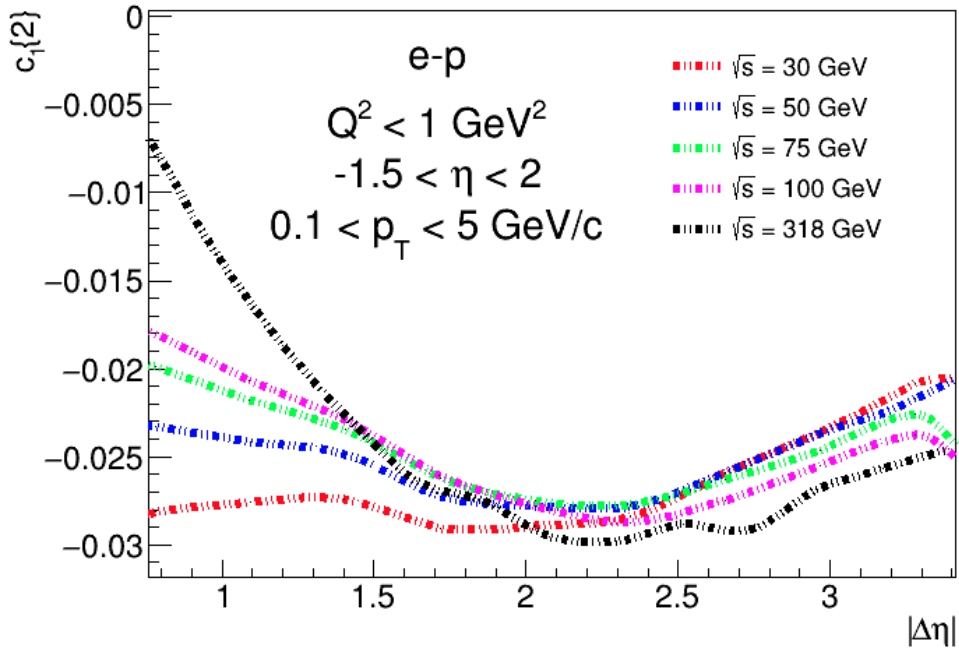
(b) Charged particle multiplicity distribution

Figure 4.5: Transverse momentum and charged particle multiplicity distribution of all final state charged particles across various center of mass energies

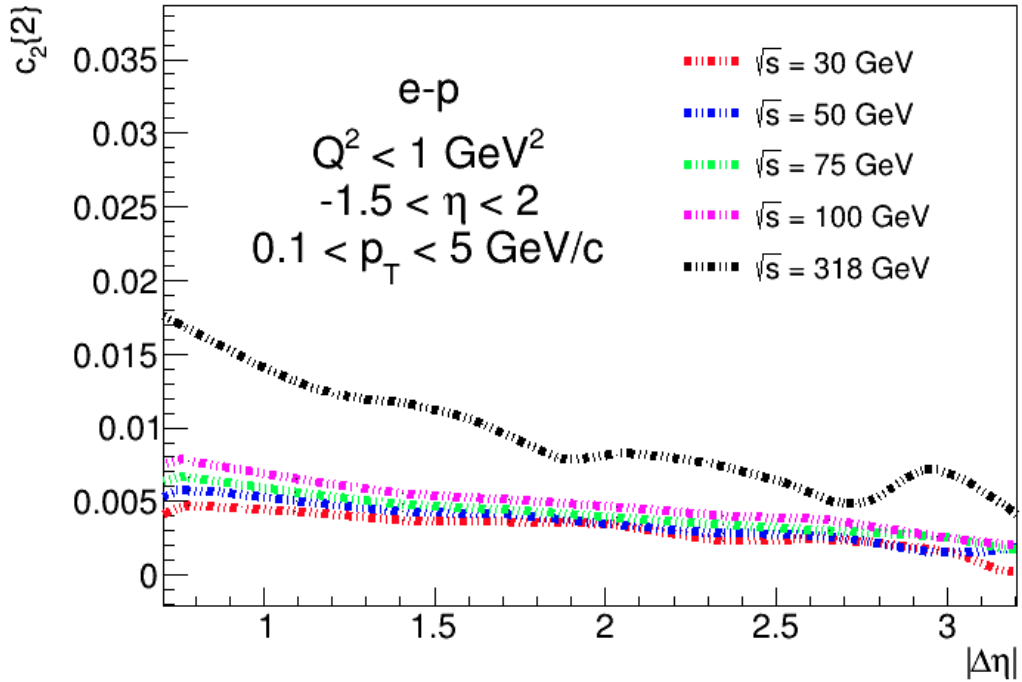
4.4 Energy dependent analysis of two-particle correlation

Figure 4.6a, 4.6b, shows the two-particle azimuthal correlation between all the final state charged particles as a function of pseudo-rapidity separation ($\Delta\eta$) at the different center of mass energies. Events with high multiplicity and particles within the, $-1.5 < \eta < 2$ and $0.1 < p_T < 5$ /c, range are selected. In figure 4.6a, we have first harmonic, $c_1\{2\}$ vs $\Delta\eta$, the correlation is negative and increases towards zero or positive, as we move to small pseudo-rapidity difference and it is seen at all the energies, another thing is the correlation strength at small pseudo-rapidity difference increases towards much negative value with the decrease in center of mass-energy. In figure 4.6b, we have second harmonic, $c_2\{2\}$ vs $\Delta\eta$, it is positive throughout the selected $|\Delta\eta|$. Here, the correlation increases with the increase in the center of mass energy, and for each energy, the correlation strength increases as we move to small pseudo-rapidity difference. Long-range correlations ($|\Delta\eta| > 2$) observed here are large and negative for $c_1\{2\}$, while being much smaller and positive for $c_2\{2\}$.

Figure 4.7a, 4.7b, shows the two-particle azimuthal correlation between all the final state charged particles as a function of average p_T ($\langle p_T \rangle$) at the different center of mass energies. The correlation $c_1\{2\}$ vs $\langle p_T \rangle$, figure 4.7a, is negative while correlation, $c_2\{2\}$ vs $\langle p_T \rangle$, figure 4.7b is positive. For both $c_1\{2\}$ and $c_2\{2\}$, the correlation strength grows with increasing $\langle p_T \rangle$, a feature that is universally observed in all collision systems.

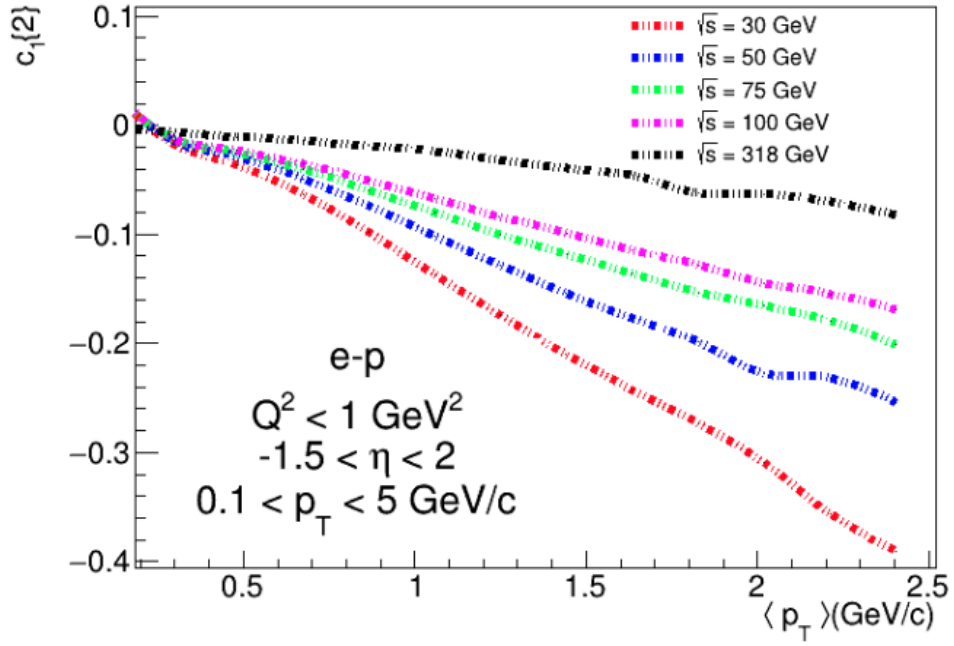


(a) $c_1\{2\}$ vs $\Delta\eta$

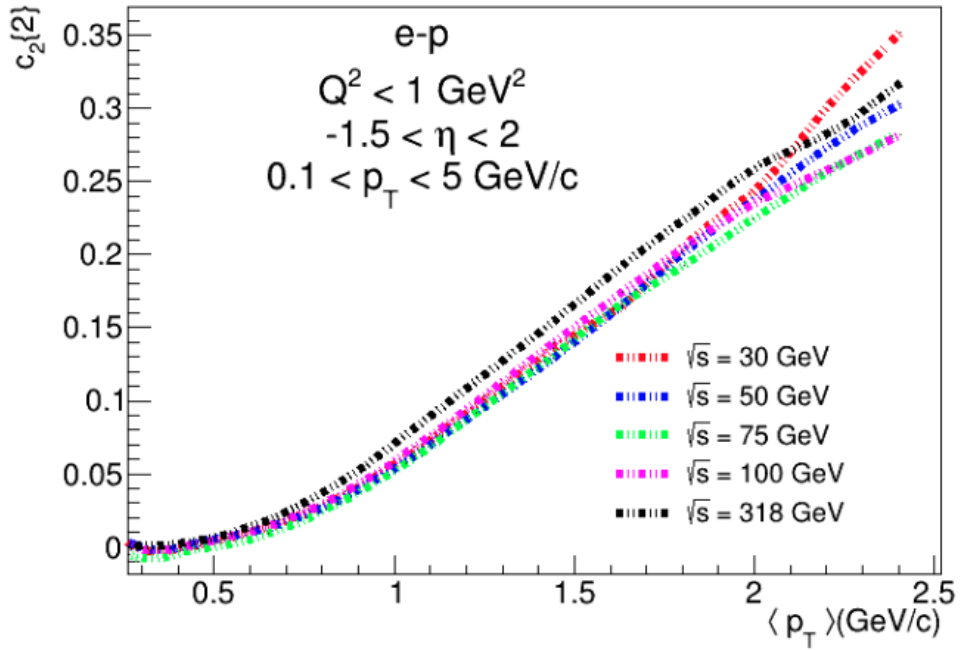


(b) $c_2\{2\}$ vs $\Delta\eta$

Figure 4.6: Two particle azimuthal correlation between all the final state charged particles across various center of mass energies



(a) $c_1\{2\}$ vs $\langle p_T \rangle$



(b) $c_2\{2\}$ vs $\langle p_T \rangle$

Figure 4.7: Two particle azimuthal correlation between all the final state charged particles across various center of mass energies

4.4.1 $\Delta\eta - \Delta\phi$ correlation

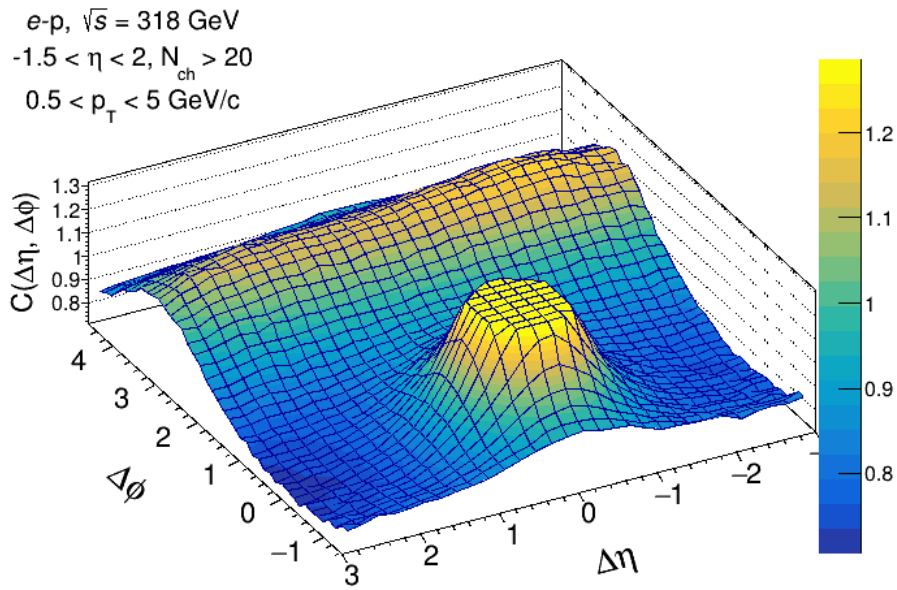
Analyzing two-particle correlations presents a robust method for investigating the mechanisms governing particle production in high-energy collisions involving hadrons and nuclei.. Such studies involve the measurement of relative angles $\Delta\phi$ and $\Delta\eta$, where $\Delta\eta = \eta_1 - \eta_2$ is the difference in pseudo-rapidity, $\Delta\phi = \phi_1 - \phi_2$ is the difference in azimuthal angle. The correlation functions are generally sensitive to different sources, for example, jets, elliptic flow, resonance decays, conservation laws, etc. These correlations create distinctive structures in $\Delta\eta - \Delta\phi$ space.

The two-particle double-differential correlation function as a function of $\Delta\eta$ and $\Delta\phi$ is defined as [11]:

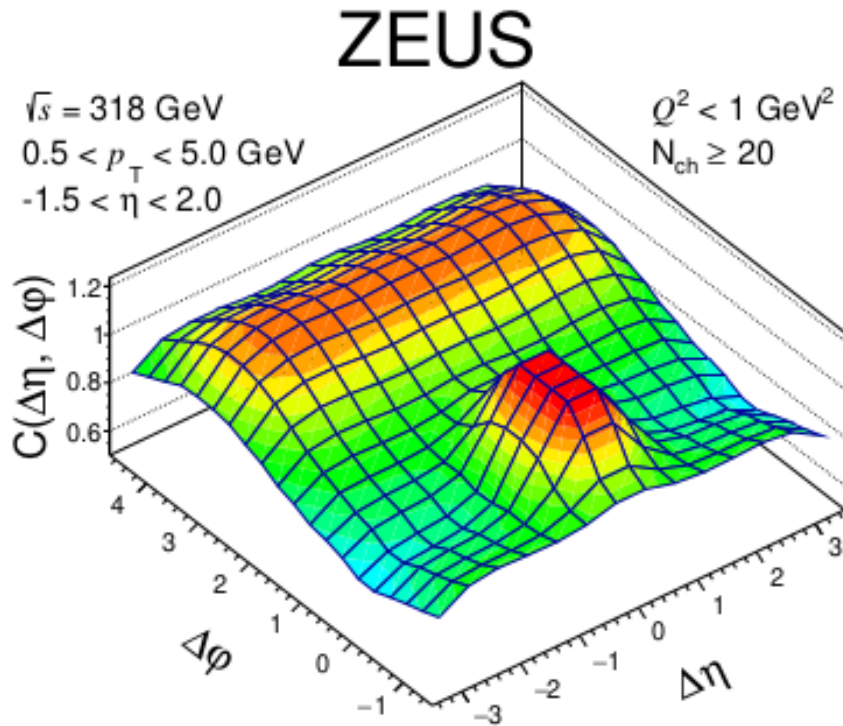
$$C(\Delta\eta, \Delta\phi) = \frac{N_{pairs}^{mixed} S(\Delta\eta, \Delta\phi)}{N_{pairs}^{same} B(\Delta\eta, \Delta\phi)} \quad (4.3)$$

where N_{same}^{pairs} is the number of pairs constructing the signal S , and N_{mixed}^{pairs} is the number of pairs in the background. The signal is determined by counting particle pairs within the same $\Delta\eta - \Delta\phi$ range in the same event. The background is estimated by applying the event mixing technique, see Appendix B.

Figure 4.8, shows the $\Delta\eta - \Delta\phi$ correlation at $\sqrt{s} = 318$ GeV, within $-1.5 < \eta < 2$ and $0.5 < p_T < 5$ GeV/c, for high multiplicity, $N_{ch} > 20$ and low $Q^2 < 1$ GeV². In figure 4.8a and 4.8b, we have the correlation from PYTHIA8 and the ZEUS experiment respectively. A dominant near-side peak ($\Delta\phi$ near 0) is seen at small $\Delta\eta$ and $\Delta\phi$. A broad ridge is observed on the other side ($\Delta\phi$ near π). The structure of $\Delta\eta - \Delta\phi$ correlation given by PYTHIA8 after mixed event correction technique, figure 4.8a, is quite similar to the one from the ZEUS experiment, figure 4.8b. The most probable reason for this kind of structure is back-to-back jets. There are two scenarios while looking at pairs of particles coming from jets. First, both particles come from the same jet. In this case, both particles are going in almost the same direction, therefore, there is a small difference between



(a) $\Delta\eta - \Delta\phi$ correlation using PYTHIA8



(b) $\Delta\eta - \Delta\phi$ correlation from ZEUS experiment

Figure 4.8: $\Delta\eta - \Delta\phi$ correlation of all charge particles at $\sqrt{s} = 318 \text{ GeV}$

their azimuthal angle, $\Delta\phi$, and also a small difference in their pseudorapidity, $\Delta\eta$. Pairs of particles from the same jet form a peak centered at $(0,0)$, called near side peak. Second, particles are from two opposite back-to-back jets. Then, $\Delta\phi$ is close to 180° . However, there is no such dependence on $\Delta\eta$. For many events and many jets, $\Delta\eta$ is uniform, producing a wide ridge at $\Delta\phi = \pi$, called an away side ridge.

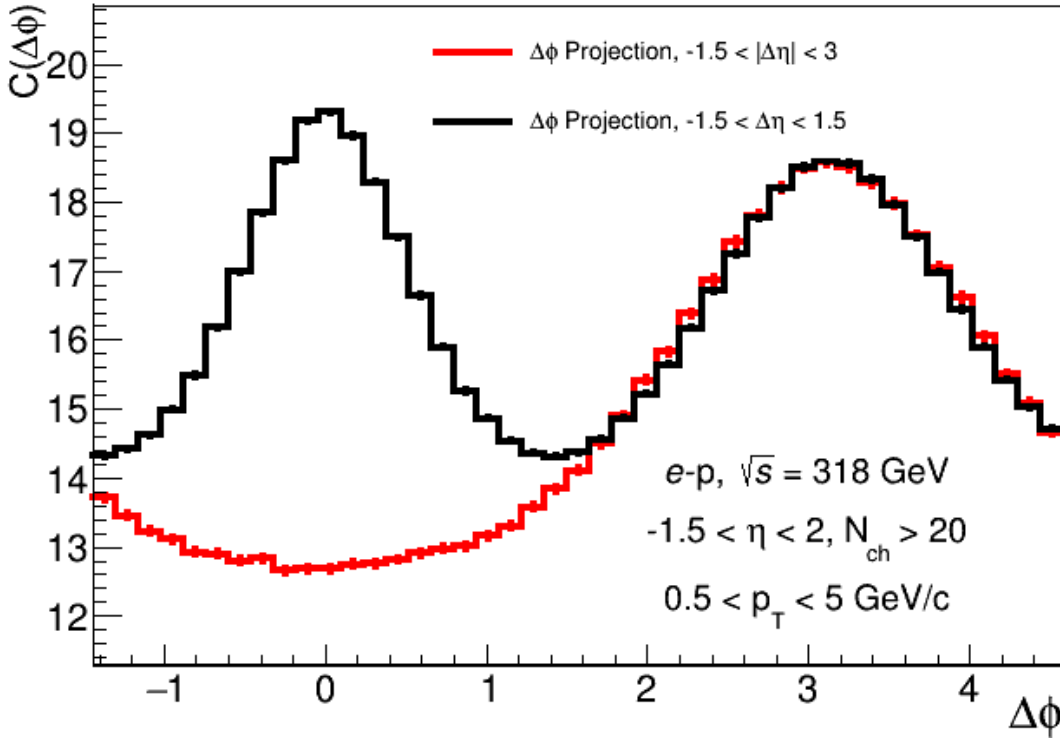


Figure 4.9: Projection of 2-D correlation function $C(\Delta\eta, \Delta\phi)$, figure 4.8, onto $\Delta\phi$ for $-1.5 < |\Delta\eta| < 3$ and $-1.5 < \Delta\eta < 1.5$ using PYTHIA8

Figure 4.9, shows the comparison between the projection of 2-D correlation function, figure 4.8 onto $\Delta\phi$, for $-1.5 < |\Delta\eta| < 3$ and $-1.5 < \Delta\eta < 1.5$. There is no indication of near side ($\Delta\phi$ near zero) ridge, which was observed in high multiplicity $p - p$ and $p - Pb$ collisions [4].

In Figure 4.11, we're looking at the $\Delta\eta - \Delta\phi$ correlation at the different center of mass energies (30-100 GeV) for high multiplicity events, simulated using PYTHIA8. At lower energies, the peak near zero $\Delta\eta$ (the near side) is

much smaller compared to the away side. However, as the collision energy increases, the correlation on the near side becomes stronger.

This change probably happens because there aren't many events with jet-like characteristics at lower energies, leading to the near-side peak being less prominent. As the energy increases, more events resemble jets, which strengthens the correlation on the near side. In figure 4.10, we have a

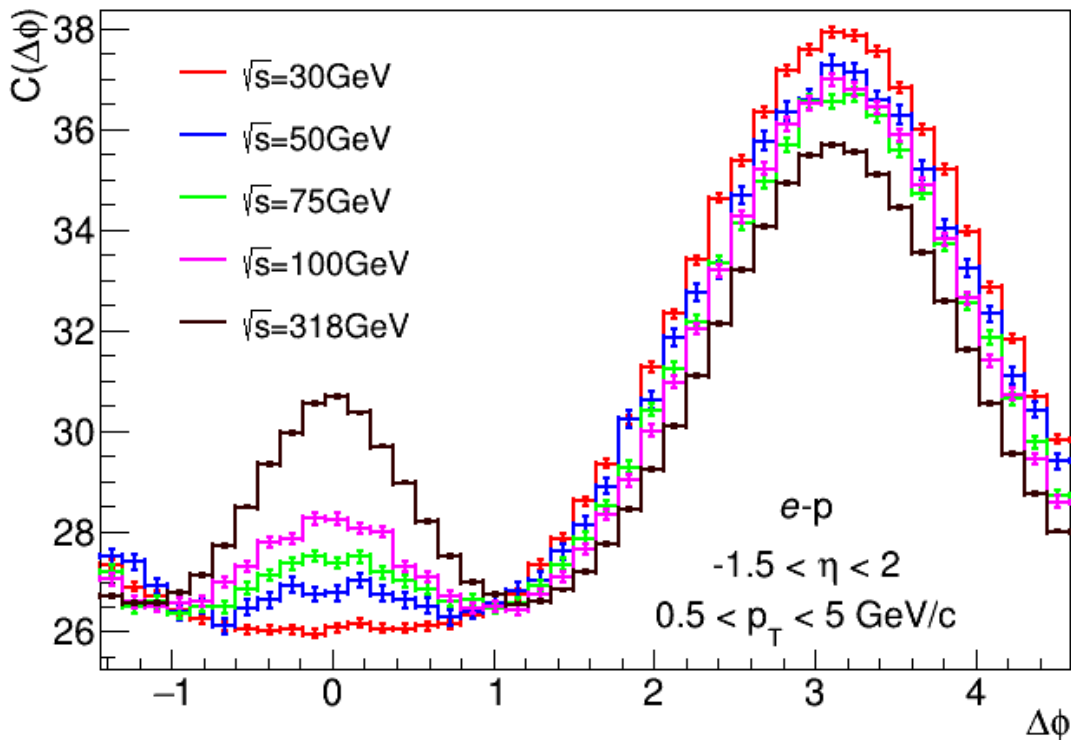
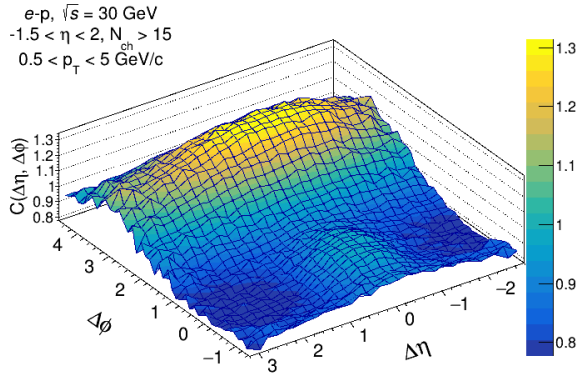
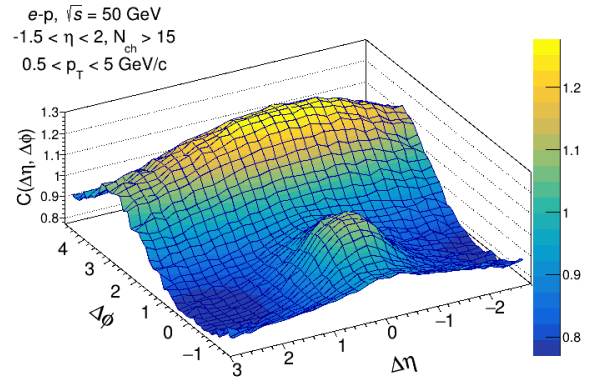


Figure 4.10: Projection of 2-D correlation function $C(\Delta\eta, \Delta\phi)$, figure 4.11, onto $\Delta\phi$ across various center of mass energies and for high multiplicity events, simulated using PYTHIA8

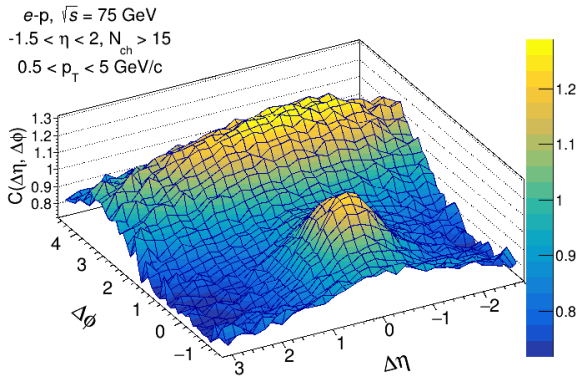
comparison between the projection of 2-D correlation function, $C(\Delta\eta, \Delta\phi)$ onto $\Delta\phi$, at different COM energies. The correlation strength on the near side increases with the increase in COM energy and on the away side it decreases. This can be clearly seen in figure 4.12, where we have the near side ($\Delta\phi \approx 0$) and away side ($\Delta\phi \approx \pi$) yield as a function of center of mass energy,



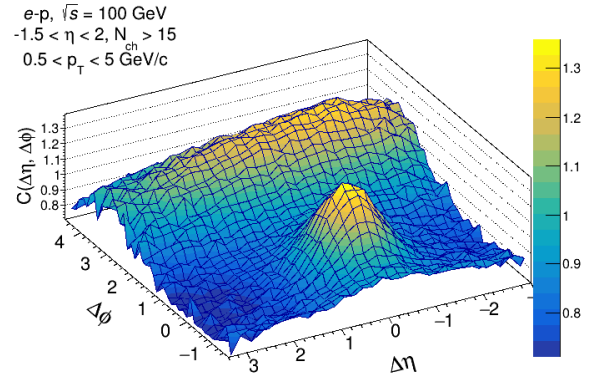
(a) $\Delta\eta - \Delta\phi$ correlation at $\sqrt{s} = 30$ GeV



(b) $\Delta\eta - \Delta\phi$ correlation at $\sqrt{s} = 50$ GeV

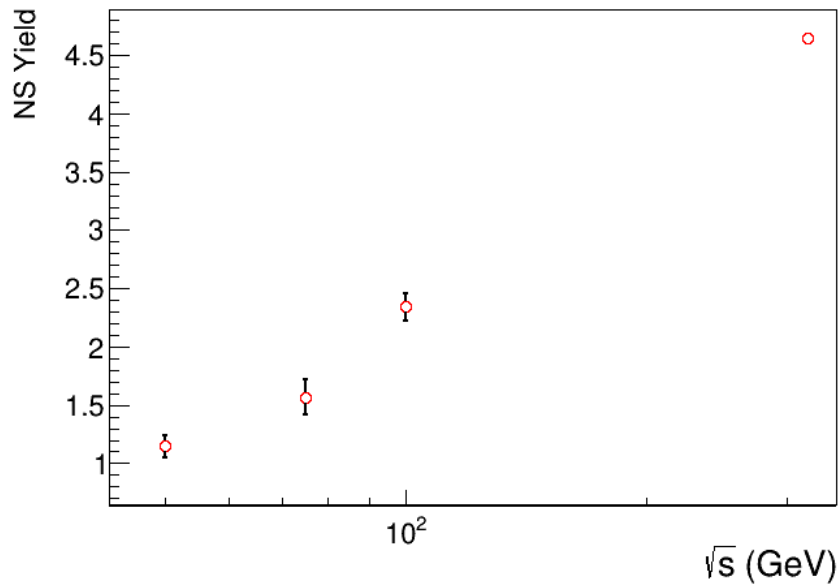


(c) $\Delta\eta - \Delta\phi$ correlation at $\sqrt{s} = 75$ GeV

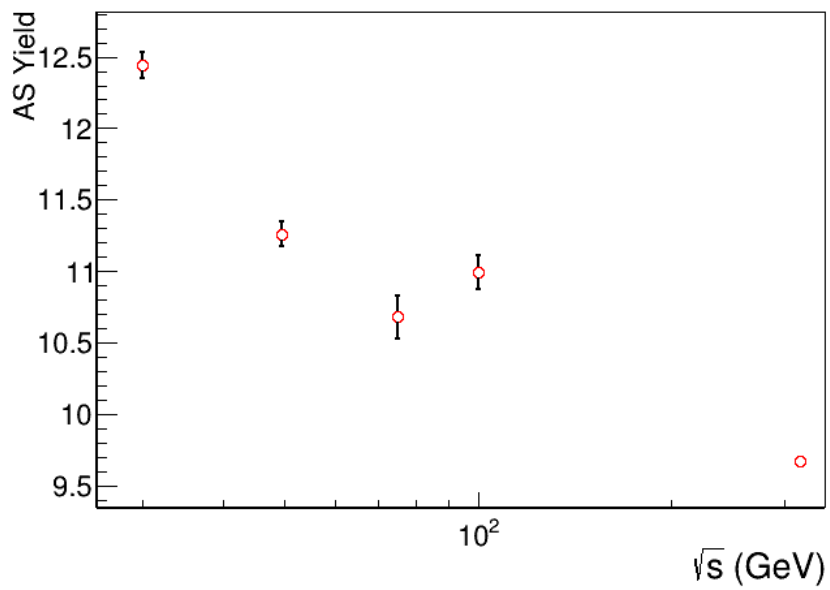


(d) $\Delta\eta - \Delta\phi$ correlation at $\sqrt{s} = 100$ GeV

Figure 4.11: $\Delta\eta - \Delta\phi$ correlation of all charge particles across various center of mass energies, using PYTHIA8



(a) Near side yield vs center of mass energy



(b) Away side yield vs center of mass energy

Figure 4.12: Near side ($\Delta\phi \approx 0$) and away side ($\Delta\phi \approx \pi$) yield as a function of center of mass energy (\sqrt{s})

Chapter 5

Summary

This thesis investigates multiple aspects within the realm of experimental particle physics, focusing on ep photoproduction and the efficiency and resolution of the ePIC detector. We start by examining how well the ePIC detector can measure particle properties like momentum and energy and it is showing good momentum resolution and efficiency. Additionally, the study encompasses fundamental kinematic analyses, including transverse momentum (p_T) and charged multiplicity spectra, for various multiple-parton interactions (MPI) scenarios using PYTHIA8 in ep photoproduction. These analyses are compared with experimental data obtained from the ZEUS experiment. The PYTHIA8 predictions with a mean MPI of 1.24 match the experimental data and demonstrate the presence of MPI in $e - p$ photoproduction. Furthermore, the two-particle correlation between charged particle pairs is studied, and their behavior across different center-of-mass energies is examined. The $\Delta\eta - \Delta\phi$ correlation is scrutinized across the variable center of mass energies, particularly investigating the presence of a ridge structure on the near side and away side in $\Delta\phi$. A ridge-like structure on the away side is present in the experimental data and PYTHIA8 also predicts the same but no near-side ridge is seen. Near side and away side yield of the $\Delta\phi$ distribution across various center-of-mass energies are studied and near side yield increases, away side yield decreases with the increasing center of mass energy.

Appendix A

PYTHIA 8 settings for photoproduction

The quark and gluon content of the proton is parameterized with the NNPDF2.3 Parton Distribution Function (PDF) at leading order [12]. Partonic fluctuations arising from the quasi-real photon are parameterized with the CJKL PDF. Parton scattering between both the PDFs in PYTHIA photoproduction is parameterized by the p_{T0} parameter. It is possible to vary a parameter p_{T0} in PYTHIA which is a lower cut-off on parton momenta and can vary the mean numbers of multiparton interactions that PYTHIA generates in its events. The energy dependence of p_{T0} is parameterized as $p_{T0} = p_{T0}^{ref} (W/7TeV)^{0.215}$ [10], where W is the center-of-mass energy of the photon-proton system, which fluctuates event-by-event. Three different levels of MPI are chosen with $p_{T0}^{ref} = 2, 3, \text{ and } 4\text{GeV}$.

Appendix B

Mixed event correction

In two-particle correlation studies, the goal is often to investigate correlations between pairs of particles originating from the same physical process, such as jet fragmentation or resonance decay. However, these signal correlations can be obscured by background correlations arising from various sources, including combinatorial effects and detector artifacts. To estimate the background correlation level, mixed events are constructed by pairing particles from different events that are statistically uncorrelated. These mixed-event pairs serve as a representative sample of the background correlation distribution. An example of the signal $S(\Delta\eta, \Delta\phi)$ and the background ($B(\Delta\eta, \Delta\phi)$) distributions as well as the correlation function $C(\Delta\eta, \Delta\phi)$ is presented in figure B.1.

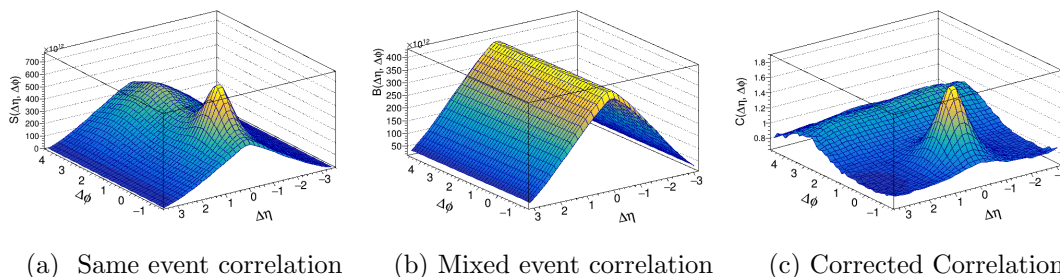


Figure B.1: Construction of the $\Delta\eta - \Delta\phi$ correlation function. Signal distribution (left), background distribution (middle), and correlation function (right).

Here is the code for mixed event correction.

```
void mixed_event_cor(){

TH2F *h1 = new TH2F("h1","Same Deta Dphi correlation", 50, -2, 5, 50, -5, 5);
TH2F *h2 = new TH2F("h2","Mix Deta Dphi correlation", 50, -2, 5, 50, -5, 5);
TH2F *h3 = new TH2F("h3","Corrected correlation", 50, -2, 5, 50, -5, 5);

//reading the root file and extracting the particle kinematics
TFile *file = new TFile("filename", "READ");

TTree *t = (TTree*)file->Get("treename");

vector<double> *Eta_1a = new vector<double>();
vector<double> *Phi_1b = new vector<double>();
vector<double> *multipliciy_1d = new vector<double>();
vector<double> *pT_1f = new vector<double>();

t->SetBranchAddress("Eta_1a", &Eta_1a);
t->SetBranchAddress("Phi_1b", &Phi_1b);
t->SetBranchAddress("multipliciy_1d", &multipliciy_1d);
t->SetBranchAddress("pT_1f", &pT_1f);

TFile *file1 = new TFile("Deta_dphi_correlation.root", "RECREATE");

int entries = t->GetEntries();
cout << entries << endl;
double eta, phi;

TRandom *rand = new TRandom(100);//random number generator
//to select a particle randomly from an event

int randEvent, mult;
const int totChgPar = 1e5; //total number of events to be mixed

double etaAllCharge[totChgPar]; //array for eta and phi
double phiAllCharge[totChgPar];

int numCharge = 0;
int i = 0;

while(i<entries){ //looping over all the events
    t->GetEntry(i);
```

APPENDIX B. MIXED EVENT CORRECTION

```

for(int j = 0; j<multipliciy_1d->size(); j++){ //for multiplicity cal
    mult = (*multipliciy_1d)[j];
    //cout << mult << endl;
}

if(mult > 15){ // for selecting high multiplicity events
    if(numCharge < totChgPar){
        //selecting a particle randomly from given event
        //and filling the eta phi info. into the arrays
        randEvent = rand->Uniform(Eta_1a->size());
        etaAllCharge[numCharge]=(*Eta_1a)[randEvent];
        phiAllCharge[numCharge]=(*Phi_1b)[randEvent];
        numCharge++;
    }
}

if(numCharge>=totChgPar){
    break;
}

i=i+1;
}

//calculating Deta, Dphi from same events
for(int n = 0; n < entries; n++){
    t->GetEntry(n);
    double DphiSame = 0;
    double DetaSame = 0;

    for(int j = 0; j<multipliciy_1d->size(); j++){
        mult = (*multipliciy_1d)[j];
        //cout << mult << endl;
    }
    if(mult > 15){
        for(int l = 0; l < Eta_1a->size(); l++){

            for(int m = l+1; m < Eta_1a->size(); m++){

                DphiSame = (*Phi_1b)[l] - (*Phi_1b)[m];
                DetaSame = (*Eta_1a)[l] - (*Eta_1a)[m];

                if(DphiSame < -(TMath::Pi())/2)
                    DphiSame = DphiSame + 2*TMath::Pi();
            }
        }
    }
}

```

```

        else if(DphiSame > 3*TMath::Pi()/2)
            DphiSame = DphiSame- 2*TMath::Pi();

            h1->Fill(DphiSame, DetaSame);
        }
    }
}

//calculating Deta, Dphi for mix events
double DphiMix = 0;
double DetaMix = 0;
for(int l = 0; l < totChgPar; l++){
    for(int m = l+1; m < totChgPar; m++){

        DphiMix = phiAllCharge[l] - phiAllCharge[m];
        DetaMix = etaAllCharge[l] - etaAllCharge[m];

        if(DphiMix < -(TMath::Pi())/2)
            DphiMix = DphiMix + 2*TMath::Pi();

        else if(DphiMix > 3*TMath::Pi()/2)
            DphiMix = DphiMix- 2*TMath::Pi();

        h2->Fill(DphiMix, DetaMix);

    }
}

//normalizing the distribution
h2->Scale(h1->GetEntries());
h1->Scale(h2->GetEntries());
h3->Divide(h1, h2, 1, 1, "");

file->Close();
file1->cd();
h1->Write();
h2->Write();
h3->Write();
file1->Write();
file1->Close();
}

```

Bibliography

- [1] T. H. Bauer, R. D. Spital, D. R. Yennie, and F. M. Pipkin. The Hadronic Properties of the Photon in High-Energy Interactions. *Rev. Mod. Phys.*, 50:261, 1978. [Erratum: *Rev. Mod. Phys.* 51, 407 (1979)].
- [2] J. Chwastowski and J. Figiel. Photoproduction at HERA. *Phys. Part. Nucl.*, 35:619–632, 2004.
- [3] G Aad and B Abbott..... Charged-particle multiplicities in pp interactions measured with the atlas detector at the lhc. *New Journal of Physics*, 13(5):053033, may 2011.
- [4] Vardan Khachatryan et al. Observation of Long-Range Near-Side Angular Correlations in Proton-Proton Collisions at the LHC. *JHEP*, 09:091, 2010.
- [5] Y. C. Chen et al. Two-particle angular correlations in e^+e^- collisions to hadronic final states in two reference coordinates at Belle. *JHEP*, 03:171, 2023.
- [6] A. Accardi et al. Electron Ion Collider: The Next QCD Frontier: Understanding the glue that binds us all. *Eur. Phys. J. A*, 52(9):268, 2016.
- [7] R. Abdul Khalek.... Science requirements and detector concepts for the electron-ion collider: Eic yellow report. *Nuclear Physics A*, 1026:122447, 2022.

- [8] The ePIC Collaboration. Electron-ion collider, <https://www.bnl.gov/eic>.
- [9] I. Abt et al. Azimuthal correlations in photoproduction and deep inelastic ep scattering at HERA. *JHEP*, 12:102, 2021.
- [10] Christian Bierlich et al. A comprehensive guide to the physics and usage of PYTHIA 8.3. *SciPost Phys. Codeb.*, 2022:8, 2022.
- [11] Małgorzata Janik. Two-particle angular correlations in pp collisions recorded with the ALICE detector at the LHC. *EPJ Web Conf.*, 71:00058, 2014.
- [12] Jacob J. Ethier and Emanuele R. Nocera. Parton distributions in nucleons and nuclei. *Annual Review of Nuclear and Particle Science*, 70(Volume 70, 2020):43–76, 2020.